Geophysical Journal International

Geophys. J. Int. (2022) **229,** 408–425
Advance Access publication 2021 November 27
GJI Gravity, Geodesy and Tides

https://doi.org/10.1093/gji/ggab482

Seasonal glacier and snow loading in Svalbard recovered from geodetic observations

H.P. Kierulf,[1,2] W.J.J. van Pelt,[3] L. Petrov,[4] M. Dähnn,[1] A.-S. Kirkvik[1] and O. Omang[1]

[1] *Geodetic Institute, Norwegian Mapping Authority, 3507 Hønefoss, Norway. E-mail: halfdan.kierulf@kartverket.no*
[2] *Department of Geosciences, University of Oslo, 0371 Oslo, Norway*
[3] *Department of Earth Sciences, Uppsala University, 752 36 Uppsala, Sweden*
[4] *NASA Goddard Space Flight Center, Greenbelt, MD 20771, USA*

Accepted 2021 November 25. Received 2021 May 10; in original form 2021 November 23

SUMMARY

We processed time-series from seven Global Navigation Satellite System (GNSS) stations and one Very Long Baseline Interferometry (VLBI) station in Svalbard. The goal was to capture the seasonal vertical displacements caused by elastic response of variable mass load due to ice and snow accumulation. We found that estimates of the annual signal in different GNSS solutions disagree by more than 3 mm which makes geophysical interpretation of raw GNSS time-series problematic. To overcome this problem, we have used an enhanced Common Mode (CM) filtering technique. The time-series are differentiated by the time-series from remote station BJOS with known mass loading signals removed *a priori*. Using this technique, we have achieved a substantial reduction of the differences between the GNSS solutions. We have computed mass loading time-series from a regional Climatic Mass Balance (CMB) and snow model that provides the amount of water equivalent at a 1 km resolution with a time step of 7 d. We found that the entire vertical loading signal is present in data of two totally independent techniques at a statistically significant level of 95 per cent. This allowed us to conclude that the remaining errors in vertical signal derived from the CMB model are less than 0.2 mm at that significance level. Refining the land water storage loading model with a CMB model resulted in a reduction of the annual amplitude from 2.1 to 1.1 mm in the CM filtered time-series, while it had only a marginal impact on raw time-series. This provides a strong evidence that CM filtering is essential for revealing local periodic signals when a millimetre level of accuracy is required.

Key words: Glaciology; Global change from geodesy; Loading of the Earth; Reference systems; Satellite geodesy; Arctic region.

1 INTRODUCTION

The Arctic archipelago Svalbard is exposed to climate change phenomena, the temperature is rising, the permafrost is melting, the sea level is rising and the glaciers are retreating (Hanssen-Bauer *et al.* 2019). Consequences of climate change, like sea level rise or increased land-uplift, can be observed by geodetic techniques in an accurate geodetic reference frame. On the other hand, these changes challenge the stability of the geodetic reference frame itself, for example the increased land uplift will deform the reference frame over time. Knowledge about the interaction between geophysical processes, crustal deformations and reference frame is mandatory to achieve the GGOS2020 goal of a reference frame with a stability of 0.1 mm yr^{-1} (Plag & Pearlman 2009).

The geodetic observatory in Ny-Ålesund is one of the core stations in the global geodetic network. It was established during the 1990s with Global Navigation Satellite System (GNSS) antennas, Very Long Baseline Interferometry (VLBI) telescope, Super Conducting Gravity (SCG), absolute gravity points and control networks (Kierulf *et al.* 2009a).

Due to Svalbard's remote location and challenging environmental conditions Ny-Ålesund was for a long time the only location with permanent geodetic equipment on the archipelago. Sato *et al.* (2006a, b) studied the gravity signal in Ny-Ålesund and the interaction between gravity changes and uplift. The uplift in Ny-Ålesund is not linear. It has a seasonal component, that will be studied in details in this manuscript, and an interannual signal induced by the long term (years to decades) evolution of glacier mass balance (e.g. Kierulf *et al.* 2009a). Kierulf *et al.* (2009b) showed that the uplift changed from year to year and that these variations are very well explained by the changes in the mass balance of the nearby glaciers. Omang & Kierulf (2011) found that also the gravity rate is

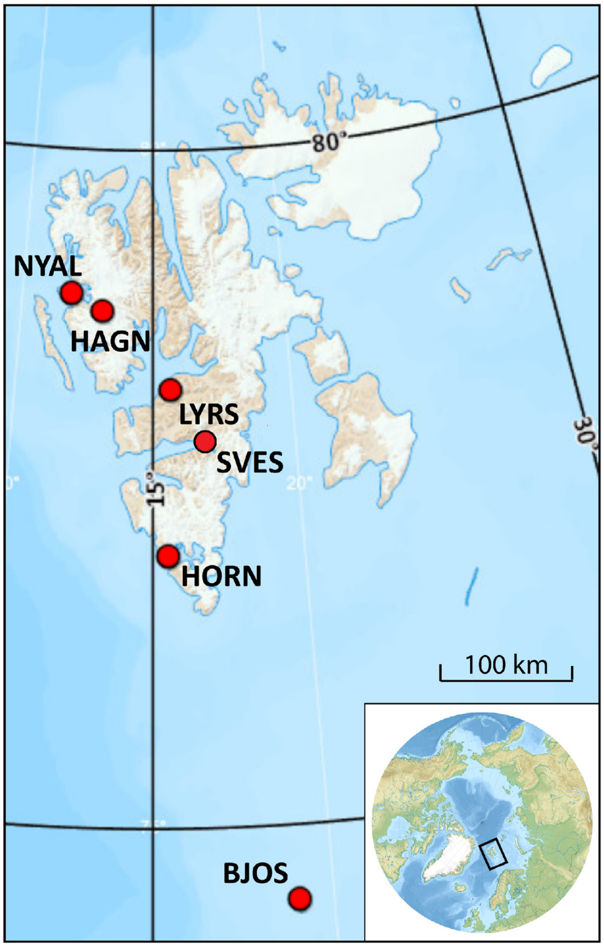

Figure 1. Geodetic network on Svalbard. The location NYAL include the GNSS stations NYAL and NYA1, the VLBI antenna NYALES20 and the SCG instrument.

changing with time. Mémin *et al.* (2012) showed that topography of glaciers has a significant effect on the gravity rate. The viscoelastic response of the last ice age (Auriac *et al.* 2016) and the viscoelastic response of the glacier retreat after the Little Ice Age (LIA, Mémin *et al.* 2014) also contribute to the uplift in Ny-Ålesund. In 2005, the Polish research station in Hornsund installed a new GNSS antenna. Rajner (2018) compared results from the stations in Hornsund and Ny-Ålesund and demonstrated that both locations have non-linear uplift. All these papers focus mainly on glacier related phenomena with time spans ranging from years to decades or thousands of years.

The most prominent variations in snowpack and glacier mass are the annual cycle with accumulation of snow each winter and melting in the short Arctic summer. The crusts elastic response of this seasonal variations results in a seasonal cycle also in the GNSS station coordinates and other geodetic equipment. The crust is also exposed to non-tidal loading (NTL) from atmosphere, ocean and land water (Petrov & Boy 2004; Mémin *et al.* 2020).

The main questions in this paper are: (1) How well do GNSS and VLBI capture the seasonal signal from glaciers and snow in Svalbard? (2) Will refining the Land Water Storage (LWS) models with a Climatic Mass Balance (CMB) model improve the loading predictions? To answer these two questions we have studied GNSS time-series from six locations on Svalbard (see Fig. 1) and the VLBI antenna in Ny-Ålesund. We have used different analysis strategies both for the GNSS and the VLBI data sets. We have also filtered our time-series for NTL and Common Mode (CM) signals to improve the regional accuracy. The model described in van Pelt *et al.* (2019) simulates glacier CMB and seasonal snow conditions, from which variations in loading from glaciers and snowpack are extracted.

In Section 2 we describe the different data sets used in this study. We describe the softwares and analysis strategies for geodetic analysis, the time-series analysis, the CM filtering and the different models used for loading predictions. In Section 3, we compare the geodetic results with the loading signal from glaciers and snow, Atmospheric (ATM), Non-Tidal Ocean (NTO) and LWS. Based on this we discuss possibilities and limitations in our solutions for revealing the seasonal elastic signal. We also study the effect of refining the hydrological model with the CMB model (Section 3.4).

2 DATA AND DATA ANALYSIS

2.1 CMB model

Glacier mass change is primarily the result of surface—atmosphere interactions (affecting snow accumulation and melt), snow processes (affecting melt water retention and run-off) and frontal processes (calving and frontal ablation of tidewater glaciers). Glacier mass changes due to atmosphere—surface—snow interactions are described by the CMB, which describes the mass change of a vertical column of snow/firn/ice, in response to surface mass, and energy exchange and run-off of melt water. The CMB dominates seasonal glacier mass change, with mass gain from snow accumulation during the cold season and melt-driven mass loss during the melt season.

Noël *et al.* (2020) have shown that for all glaciers in Svalbard the mass fluxes of precipitation (+23 $\mathrm{Gt\,yr^{-1}}$) and run-off (–25 $\mathrm{Gt\,yr^{-1}}$) dominate the seasonal climatic mass balance cycle in recent decades (1985–2018), with nearly all run-off concentrated in the summer months (June, July and August) and snow accumulating the rest of the year. These mass fluxes are much larger than the estimated mean ice discharge due to calving and frontal ablation from tidewater glaciers (7 $\mathrm{Gt\,yr^{-1}}$, Błaszczyk *et al.* 2009). Svalbard-wide constraints on the seasonality of combined calving and frontal ablation are currently lacking and not considered here. Previous estimates on three glaciers in Svalbard however indicate that frontal ablation is more substantial in summer and early autumn than during winter and spring (Luckman *et al.* 2015).

Here, we use the CMB model data set, described in van Pelt *et al.* (2019), and extract weekly output for the period 1990–2018. van Pelt *et al.* (2019) used a coupled energy balance—subsurface model (van Pelt *et al.* 2012) to simulate CMB for all glaciers in Svalbard, as well as seasonal snow conditions in non-glacier terrain. Both the glacier and seasonal snow mass changes are accounted for. They describe weekly mass changes resulting from snow accumulation, surface moisture exchange, melt and rain water refreezing and retention in snow, and run-off. Run-off estimates are local and no horizontal transport of water is accounted for.

2.2 Elastic loading signal

Mass redistribution results in Earth's crust deformation called mass loading (Darwin 1882). Mass loadings are caused by the ocean water mass redistribution due to gravitational tides and pole tide (ocean tidal loading), by variations of the atmospheric mass (ATM loading), by variations of the bottom ocean pressure due to ocean circulation (NTO loading), and by variations of land water mass stored in soil, snow and ice (LWS loading). Mass loading crustal deformations have a typical magnitude at a centimetre level (see e.g. Petrov & Boy 2004).

Love (1911) showed that the deformation caused by mass loadings can be found in a form of an expansion into spherical harmonics. Each spherical harmonic of the deformation field is proportional to the spherical harmonic of the surface pressure exerted by loading mass. The proportionality dimensionless coefficients called Love numbers that depend on a harmonic degree are found by solving differential equations. Therefore, when the global pressure field mass redistribution is known, the elastic deformation can be found by expansion of that field into spherical harmonics, scaling the harmonics by Love numbers and performing an inverse spherical harmonics expansion.

Love numbers were computed using the REAR software (Melini *et al.* 2015) for the Earth reference model STW105 (Kustowski *et al.* 2008). Time-series of NTL from ATM, NTO and LWS have been used in our analysis. Input to the ATM loading is the pressure field from NASA's numerical weather model MERRA2 (Gelaro *et al.* 2017). The NTO loading uses the model MPIOM06 (Jungclaus *et al.* 2013), and the LWS loading uses the pressure field of MERRA2 model (Reichle *et al.* 2011). The MERRA2 model accounts for soil moisture at the depth of 0–2 m and accumulated snow. 3-D displacements cause by these loadings were computed using spherical harmonics transform of degree and order 2699 and presented at a global grid $2' \times 2'$ with a time step of 3 or 6 hr. Then mass loading at a given station is found by interpolation. The time-series of these loadings are available at the International Mass Loading Service http://massloading.net (Petrov 2017).

However, the MERRA2 numerical weather model do not adequately describe accumulation and run-off of water, snow, and ice at glaciers. It does not consider all complexity of glacial mass change processes and its resolution, 16 × 55 km, is insufficient to catch fine details in Svalbard. Here, we test the impact of replacing the above global model component for snow and ice with the regional snow and glacier CMB product with 1 × 1 km resolution. The model is described in Section 2.1. We have regridded the 1 × 1 km model to a uniform, regular, latitude–longitude grid with a resolution of $30'' \times 30''$. The model value at a given element of the new grid is

$$M_{ij} = \frac{\sum\limits_{ab} M_{ab} e^{-r_{ij,ab}/D}}{\sum\limits_{ab} e^{-r_{ij,ab}/D}}, \tag{1}$$

where M_{ab} is the model value for element a,b, the $r_{ij,ab}$ is the distance between gridpoints i,j and a,b and D is the kernel distance set to 1 km.

We have computed mass loading time-series, from 1990-08-05 through 2018-08-26 with a step of 7 d, at a $30'' \times 30''$ grid from the CMB output using spherical harmonic expansion degree and order 10 799. This high resolution was used to correctly model the signal at stations that are located close to the edge of glaciers.

The choice of the degree/order of the expansion is determined by availability of computing resources. The higher degree/order of the spherical harmonic transform, the less errors near the coastal line. Atmospheric, land-water storage and non-tidal ocean loading are computed with the time resolution of 3 hr and the total computation time using degree/order 2699 is about 4 yr per single core for CPUs produced in 2015–2020. Since the glacier model has time resolution of 7 d we can afford to run computation with degree/order 10799 which allows to correctly model the signal at stations that are located close to the edge of glaciers.

However, it is not sufficient to replace the LWS loading computed on the basis of MERRA2 model with the mass loading computed on the basis of the CMB model. Crustal deformation at a given point is affected by mass loading not only from the close vicinity, but also from remote areas. Therefore, in order to account for loading displacement caused by mass redistribution from the area beyond Svalbard archipelago, we computed an additional series of LWS loading using MERRA2 model that was set to zero outside Svalbard archipelago. The total LWS loading displacement is:

$$D_{\mathrm{LWS}} = D_{\mathrm{merra2}} - D_{\mathrm{merra2,svalbard}} + D_{CMB}, \tag{2}$$

where D_{merra2} is the displacement from MERRA2 model, $D_{\mathrm{merra2,\,svalbard}}$ is the loading signal from the MERRA2 model that was set to zero except latitude $76° < \phi < 81°$ and longitude $10° < \lambda < 34°$ (the area including the Svalbard archipelago) and D_{CMB} is the displacement form the CMB model.

Fig. 2 shows the high-resolution maps of the rate and amplitude of the annual signal in crustal deformation caused by the water mass change in Svalbard archipelago according to the CMB model. The parameters were estimated in a 4-parameter least square regression (mean value, rate and sine and cosine annual term) for the time-series in each gridpoint.

2.3 GNSS data analysis

In this study, we have used 30 s daily RINEX data resampled to 5 min, from five permanent GNSS stations on Svalbard (NYAL, NYA1, LYRS, SVES and HORN), and one station on Bear Island (BJOS) 240 km south of Svalbard (see Fig. 1). All stations are located close to existing settlements with infrastructure like power supply and communication. We have also used data from station, HAGN, located at a nunatak in the middle of the glacier Kongsvegen 30 km southeast of Ny-Ålesund. This station is powered by solar panels and batteries. In the dark season, data is recorded for 24 hr once a week to save power until the sun is back. Data is downloaded during a field trip once a year.

GNSS data are analysed with the program packages Gamit/Globk (Herring *et al.* 2018) and GipsyX (Bertiger *et al.* 2020). The GipsyX software is using undifferentiated observations. We are using the Precise Point Positioning (PPP) approach (Zumberge *et al.* 1997) and the solutions are in the International GNSS Service (IGS) realization of International Terrestrial Reference Frame (ITRF2014, Altamimi *et al.* 2016) through the Jet Propulsion Laboratory (JPL) orbit and clock products. We distinguish between the GispyX-FID and GipsyX-NNR solution, whereby either JPL fiducial (FID) or No-Net-Rotation (NNR) orbit and clock products are applied. The NNR products are only constrained via three no-net-rotation parameters to the ITRF2014 solution, whereas the FID products are tied in addition with three translation and one scale parameter to ITRF2014 (Bertiger *et al.* 2020). Gamit software uses double difference observations. To ensure a good global realization in ITRF2014 of the Gamit solution a global network of approximately 90 global IGS stations was analysed and combined with the Svalbard stations before transforming to ITRF2014. The global stations were all stable stations with long time-series. Daily coordinate time-series are extracted from these solutions.

The two stations in Ny-Ålesund belong to the IGS network and are analysed by several institutions, University of Nevada, Reno (UNR, Blewitt *et al.* 2018), JPL (Heflin *et al.* 2020) and Scripps Orbits and Permanent Array Center (SOPAC, Bock & Webb 2012). NYAL and NYA1 are also included in the latest ITRF2014 (Altamimi *et al.*

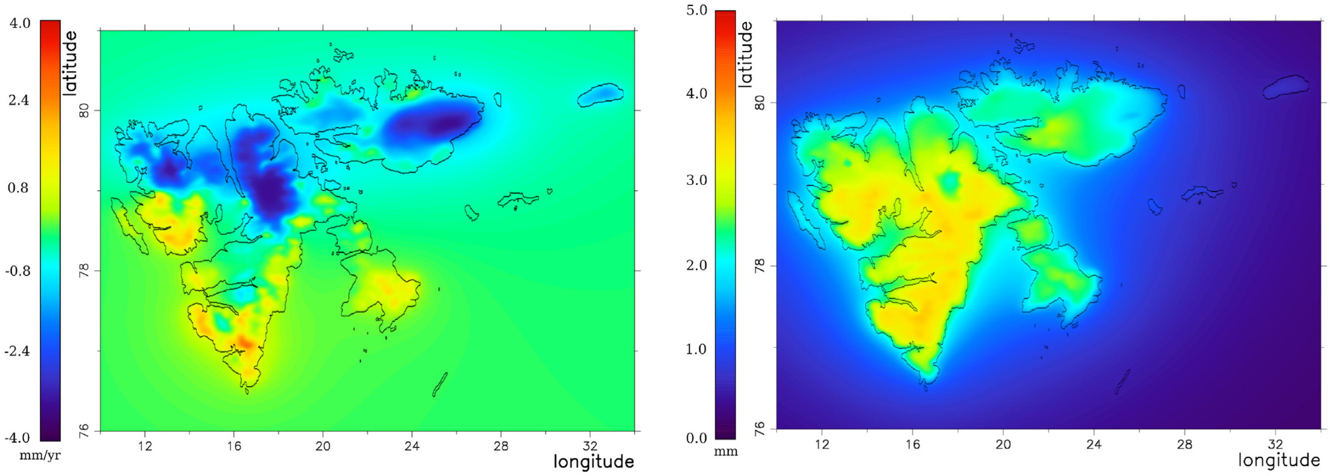

Figure 2. Crustal deformations due to glacier and snow loading according to the CMB model. The panels are: the rate of change (left-hand panel) and annual signal (right-hand panel). Important: the CMB model does not account for mass loss due to frontal ablation and calving.

2016) solution. Key parameters for the different analysis strategies are given in Table 1.

The time-series are analysed with Hector software (Bos *et al.* 2008). We have used the following model function:

$$h(t) = A + Bt + \sum_{j=1}^{2} C_j cos(j2\pi t - \phi_j), \qquad (3)$$

where A is the constant term, B is the rate, C_j is the amplitudes of the sinusoidal constituents and ϕ_j is the corresponding phases. We have assumed that the temporal correlation in the time-series are a combination of white noise and flicker noise. We have used data from 2010-01-01 until 2018-10-01 in all the GNSS results and comparisons. This limited time period ensures that we have the same time period for all the stations (except HAGN which was established in 2013), no breaks due to equipment shift, and the time-series overlap with the CMB model (see Section 2.1).

The time-series for the vertical component of the Gamit-NMA solution is plotted in Fig. 3.

2.4 VLBI

The VLBI station NYALES20 participated in 2183 twenty-four hour observing sessions from 1994-10-04 to 2020-10-19. We ran several solutions.

Solution s1 was obtained using the geodetic analysis software Where (see Kirkvik *et al.* 2017 for more details). VLBI observing sessions were individually analysed with the following approach: *a priori* station coordinates were taken from ITRF2014 including the post-seismic deformation models or VTRF2019d (IVS update of ITRF2014) for newer stations. To define the origin and the orientation of the output station position estimates, tight no-net-translation and no-net-rotation with respect to ITRF2014 were imposed. *A priori* radio source coordinates were taken from the ICRF3 S/X catalogue (Charlot *et al.* 2020) and corrected for the galactic aberration. The source coordinates were not estimated. *A priori* Earth orientation parameters were taken from the C04 combined EOP series consistent with ITRF2014. The Earth orientation parameters, polar motion, polar motion rate, UTC-UT1, length of day, and celestial pole offsets, were then estimated for each session. In addition, troposphere and clock parameters was estimated. Key parameters for the VLBI solutions are included in Table 2.

Solution s2 was obtained using VLBI analysis software suite pSolve (http://astrogeo.org/psolve). Source position, station positions, station velocity, sinusoidal position variations at annual, semi-annual, diurnal, semi-diurnal frequencies of all the stations, were estimated as global parameters in a single least square solution using all dual-band ionosphere-free combinations of VLBI group delays from 1980-04-12 to 2020-12-07, in total 14.8 million observations. There are 28 stations that have discontinuities due to seismic events or station repair. These discontinuities and associated non-linear motion was modeled with B-splines with multiple knots, and the B-spline coefficients were treated as global parameters. In addition to global parameters, the Earth orientation parameters, pole coordinates, UT1, their first time derivatives, as well as daily nutation offsets are estimated for each observation session individually. Atmospheric zenith path delay and clock function are modeled with B-splines of the 1st degree with time span 60 and 20 min, respectively. A so-called minimum constraints on station positions and velocities and source coordinates were imposed to invert the matrix of the incomplete rank. These constraints require that the net translation and rotation station positions and velocities of a subset of stations be the same as in ITRF2000 catalogue and net rotation of the so-called 212 defining sources be the same as in ICRF. It should be noted that s2 solution is independent on the choice of the *a priori* reference frame, that is change in the *a priori* position does not affect results.

The data reduction model included modeling thermal variation of all antennas, oceanic tidal, NTO ATM and LWS loading with one exception, where for station NYALES20 the following LWS model were used $D_{\mathrm{merra}} - D_{\mathrm{merra,\ svalbard}}$. Implying that the *a priori* model totally ignores mass loading exerted by water mass redistribution in Svalbard.

The VLBI network is small and heterogeneous: different stations participate in different experiments. Therefore, the time-series of station position should be treated with a great caution: the estimate of the position change of station X affects the position estimate of station Y because of the use of the net translation and net rotation constraints to solve the system of the incomplete rank. An alternative approach to processing time-series is estimation of admittance

Table 1. GNSS analysis strategies. (∗) Elevation dependent site by site functions, where *a* and *b* are estimated based on postfit editing of residuals from each station. *E* is the elevation angle.

	Gamit-NMA	GipsyX-FID	GipsyX-NNR	Gamit-SOPAC	GipsyX-UNR	GipsyX-JPL
Orbit and clock product	Estimated	JPL fiducial	JPL-NNR	Estimated	JPL-NNR	JPL-NNR
Elevation angle cut-off	10°	7°	7°	10°	7°	7°
Elevation dependent weighting	$a^2 + b^2/\sin(E)^2$ (∗)	$1/\sqrt{\sin(E)}$	$1/\sqrt{\sin(E)}$	$a^2 + b^2/\sin(E)^2$ (∗)	$1/\sin(E)$	$1/\sqrt{\sin(E)}$
Troposphere mapping function	VMF1	VMF1	VMF1	VMF1	VMF1	GPT2w
2nd order ionosphere model	IONEX from CODE	IONEX from JPL	IONEX from JPL	IONEX from IGS	IONEX from JPL	IONEX from JPL
Solid Earth tide	IERS2010	IERS2010	IERS2010	IERS2010	IERS2010	IERS2010
Ocean tidal loading	FES2004	FES2004	FES2004	FES2004	FES2004	FES2004
Ocean pole tide	IERS2010	IERS2010	IERS2010	IERS2010	IERS2010	Not applied
Ambiguity	Resolved	Resolved	Resolved	Resolved	Resolved	Resolved

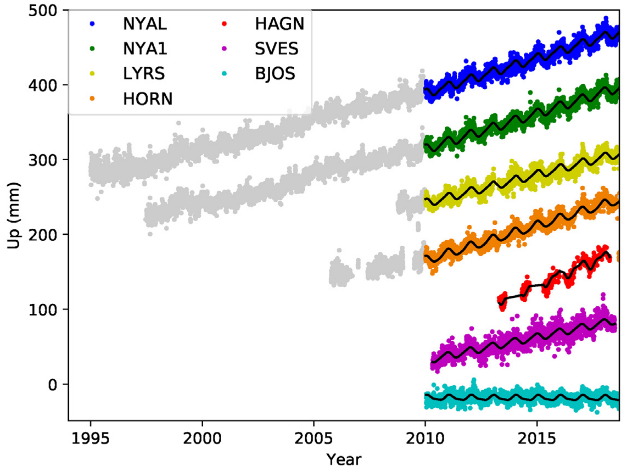

Figure 3. GNSS vertical time-series for the Gamit-NMA solutions. The color coded time span is the data period used in this study. The black curves are the model function fitted to this period. The HORN station was moved to a new location in 2009. The time-series are shifted with respect to each other to improve readability.

factor. We assume that the time-series of the displacement in question $d(t)$ is present in data as $a \cdot d(t)$ where a is a dimensionless parameter called an admittance factor that is assumed constant for the time period of observations. The admittance factor describes what share of the modeled signal is present in observations.

We noticed that seasonal crustal deformations of NYALES20 positions are periodic but not sinusoidal. The shape of these variations is surprisingly stable with time (Fig. 4). We decomposed the mass loading signal into four components: seasonal, interannual, linear trend, and residuals. The decomposition was performed in three steps. First, the mass loading time-series were filtered with the low-pass Gaussian filter, which provided a coarse interannual signal (IAV(t)). Secondly, the time-series were folded of the phase in a form $p = (t - t_0)/\Delta t$, where t is time, t_0 is the reference epoch 2000.0, Δt is the period (1 yr), and then smoothed. That provided a coarse estimate of the seasonal signal [SEA(t), blue curve in Fig. 4]. Then we adjusted parameters A, B, a_i, s_i of the decomposition of the loading displacements $D(t)$ described by the eq (4), using a single least square solution:

$$D_{\mathrm{CMB}}(t) = \mathrm{IAV}(t) + \mathrm{SEA}(p(t)) + A + Bt + \varepsilon(t), \tag{4}$$

where

$$\mathrm{IAV(t)} = \sum_i a_i B_i(t)$$

$$\mathrm{SEA(t)} = \sum_i s_i B_i(p(t)),$$

where B_i is the basis spline of the 3rd degree with the pivotal knot i.

Fig. 4 illustrates the seasonal component of the loading signal at NYALES20. A thin red line at the plot shows result of the best fit of the sinusoidal signal. However, the sinusoidal model provides a poor fit to the data with errors reaching 40 per cent of the seasonal signal. All constituents of this expansion for NYALES20 are shown in Fig. 5.

In solution s3 we did not estimated annual and semi-annual sinusoidal variations of NYALES20 positions, but estimated admittance factors for the up, east, and north components of the IAV(t) + SEA($p(t)$) mass loading time-series. In contrast to estimation of sinusoidal variations, the shape and phase of the signal remains fixed when we estimate admittance. The adjusted parameter is the scaling factor of the modeled displacement magnitude. The power of this approach is that it allows us to evaluate quantitatively the amount of the modeled signal in data, and test a statistical hypothesis that all model signal is present in the data.

The results of admittance factor estimation are presented in Table 3 in row ADM_TOT. Then we estimated the admittance factor for the seasonal SEA[$p(t)$] and interannual variations IAV(t) separately in the s4 solution.

2.5 Gravimetry/SCG

We use gravity measurements from two SCG instruments covering the period 1999 to 2018 to estimate gravity change. Gravity measurements from 1999 to 2013 and 2014 to 2018 are collected with C039 and iGrav012 SCG instrument, respectively. The original gravity measurements have a spacing of 1 second, giving a total of approximately 620 million measurements. They are resampled every minute using a symmetric numerical Finite Impulse Response (FIR) zero phase low-pass filter with a cut-off at 120 s (Wenzel 1996). Data was then cleaned for outliers and earthquakes. We corrected for the effect of air pressure using the value of $-0.422 \pm 0.004\ \mu\mathrm{Gal\,hPa^{-1}}$ found by Sato *et al.* (2006a). Both the solid earth and ocean tides are removed from the gravity data by estimating a synthetic tide based on Hartmann & Wenzel (1995) tidal model and a set of tidal parameters. The synthetic tide is estimated using ETERNA 3.4 (Wenzel 1996).

We also estimated and removed the instrumental drift by comparing to absolute gravity measurements. We estimated a linear drift (using unweighted least squares) by comparing to ten AG measurements (2000, 2001, 2002, 2004, 2007, 2010, twice in 2012, 2014, 2017). The estimated value is $-2.74107 \pm 0.17\ \mu\mathrm{Gal\,yr^{-1}}$. Finally, we re-sampled the data first every 5 min and then every 1 hr using a symmetric FIR zero phase filter (cut-offs 1250 s and 2 hr, respectively) and then to daily values using a flat filter.

Table 2. VLBI analysis strategies.

	Where	pSolve
A priori radio source coordinates	ICRF3 S/X	Solved for
A priori EOP	C04 combined	Solved for
Elevation angle cut-off	0°	5°
Troposphere mapping function	VMF1 (Boehm *et al.* 2006)	Direct integration Using output of Numerical weather Model GEOS-FPIT
Solid Earth tide	IERS2010	Elastic (Mathews *et al.* 1997)
Ocean tidal loading	TPXO7.2	FES2014B
Ocean pole tide	IERS2010	IERS2010
Higher order ionosphere	Not applied	Applied

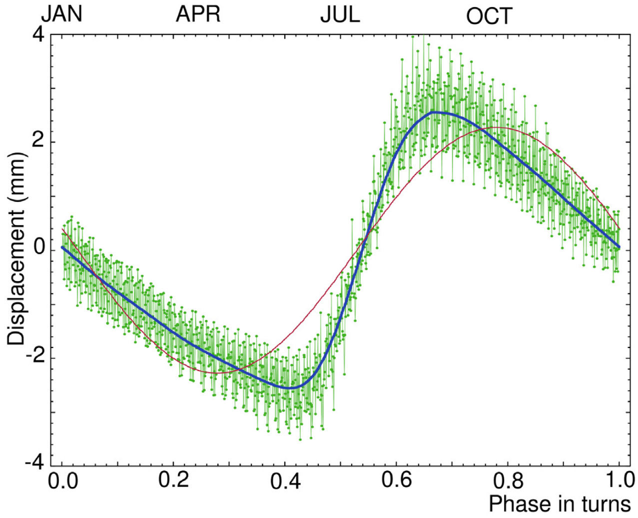

Figure 4. Folded periodic up LWS mass loading displacements of NYALES20 after removal of the slowly varying constituent. The thick blue line shows the estimate of the seasonal constituent. Green dots show the mass loading signal after removal of the interannual constituent. A red thin line shows a sinusoidal fit in a form $a \cos 2\pi\ p + b \sin 2\pi\ p$, where p is the phase of the seasonal signal in turns.

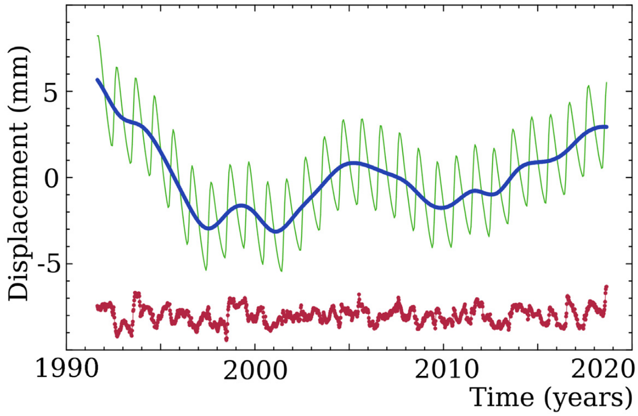

Figure 5. Three constituents of the vertical LWS mass loading at station NYALES20. The thick blue line shows the interannual variation, the green thin line shows the seasonal component, and red dots in the bottom shows the residual signal. The residual signal is artificially shifted by –8 mm. The linear trend is removed and not shown.

Table 3. Admittance factors of NYALES20 displacements caused by LWS loading. The first row, ADM_TOT shows the admittance factor estimate from s3 solution of the total mass loading signal. Rows ADM_SEA and ADM_IAV shows estimates of the seasonal and interannual constituents of the loading signal from s4 solution respectively.

Factor	Up	East	North
ADM_TOT	1.38 ± 0.04	0.62 ± 0.05	2.05 ± 0.12
ADM_SEA	1.10 ± 0.05	0.47 ± 0.11	6.10 ± 0.49
ADM_IAV	2.90 ± 0.07	2.44 ± 0.11	1.00 ± 0.15

2.6 Filtering of Common Mode and elastic loading signal

It is well known that stations in a region can have a spatially correlated signal, a so-called CM signal (Wdowinski *et al.* 1997), and that removal of the CM signal can reduce noise in the time-series. The CM signal could come from the GNSS analysis strategy and from the strategy for reference frame realization. It could come from mismodelled orbit, clocks or EOPs, or through unmodelled large scale hydrology or atmospheric effects. To remove such signal either CM filtering, Empirical Ortoghonal Functions (EOF) or regional reference frame realization, can be used. All these methods presuppose that we have stations exposed to the same undesirable CM signal. In Arctic areas, we have limited access to nearby stations. All stations on Svalbard are exposed to similar signals from glaciers, using one or several of these stations for removal of the CM signal will not only remove the CM signal, but also the real elastic signal from snow and ice.

The station BJOS at Bear Island is located 240 km south of Svalbard. The Island is small and surrounded by ocean and the local loading signal from ice and snow is approximately 10 per cent of the signal in Ny-Ålesund (see Tabel A2). It is the closest GNSS station outside Svalbard. Time-series of the BJOS station are used to estimate the CM signal. Time-series for the BJOS station, and hence CM filtering, are only included in the solutions computed by the authors (Gamit-NMA, GipsyX-FID and GipsyX-NNR) and not available in the external solutions (SOPAC, JPL, UNR and ITRF). The CM filtered time-series for the ith station is then:

$$H^i_{\mathrm{CM}}(t) = H^i_{\mathrm{GNSS}}(t) - \mathrm{CM}(t) = H^i_{\mathrm{GNSS}}(t) - H^{\mathrm{BJOS}}_{\mathrm{GNSS}}(t), \qquad (5)$$

where t is the epoch and H^i_{GNSS} and $H^{\mathrm{BJOS}}_{\mathrm{GNSS}}$ is the time-series for station i and BJOS, respectively.

The CM filtering removes the common error signal at the stations as well as real measured signal at BJOS. If the station at Bear Island has an unique unmodelled loading signal not present in other Svalbard stations, this unique signal will be erroneously subtracted also from the other stations.

Table 4. Trend, annual- and semi-signal in Ny-Ålesund and Bear Island. The parameters are estimated trend and annual signal estimated using eq. (3). The results are for different GNSS solutions, VLBI, SCG and NTL in Ny-Ålesund and Bear Island. In the VLBI time-series a pure white noise model is assumed. The gravity values (∗) are converted to millimeter using the convertion ratio –0.24 μGal mm^{-1} from Mémin *et al.* (2012). CM is the CM filtered time-series described in Section 2.6. NTL is the sum of non tidal elastic loading signal from ATM, NTO and LWS including the load from snow and glacier from the CMB model.

Station		Trend (mm yr^{-1})	Annual signal		Semi-annual signal	
			Amp. (mm)	Pha. (°)	Amp. (mm)	Pha. (°)
NYA1	Gamit-SOPAC	9.61 ± 0.62	6.28 ± 0.64	–51.3 ± 5.8	1.71 ± 0.44	107.1 ± 14.6
	Gamit-NMA	9.62 ± 0.62	5.80 ± 0.64	–13.0 ± 6.3	1.42 ± 0.44	57.6 ± 17.2
	GipsyX-FID	9.49 ± 0.69	3.05 ± 0.70	–45.7 ± 13.0	1.05 ± 0.45	123.1 ± 23.2
	GipsyX-NNR	9.26 ± 0.67	2.96 ± 0.69	–27.4 ± 13.1	0.91 ± 0.42	134.0 ± 24.8
	GipsyX-UNR	9.27 ± 0.67	2.91 ± 0.69	–27.6 ± 13.3	0.91 ± 0.42	135.2 ± 24.8
	GipsyX-JPL	9.59 ± 0.65	3.36 ± 0.66	–12.9 ± 11.1	1.08 ± 0.43	161.5 ± 21.9
	ITRF2014	9.00 ± 0.95	4.05 ± 0.75	–36.2 ± 10.5	1.08 ± 0.47	157.5 ± 23.6
	Gamit-NMA (CM)	9.55 ± 0.36	4.07 ± 0.38	–47.5 ± 5.4	0.66 ± 0.26	113.1 ± 21.3
	GipsyX-FID (CM)	9.80 ± 0.31	2.84 ± 0.34	–54.0 ± 6.8	0.86 ± 0.24	136.5 ± 15.9
	GipsyX-NNR (CM)	9.86 ± 0.35	2.91 ± 0.38	–58.2 ± 7.4	0.82 ± 0.27	127.9 ± 18.1
NYAL	Gamit-SOPAC	9.41 ± 0.61	6.24 ± 0.63	–56.6 ± 5.8	1.96 ± 0.44	105.8 ± 12.7
	Gamit-NMA	9.57 ± 0.67	5.22 ± 0.69	–12.9 ± 7.6	1.75 ± 0.48	64.3 ± 15.4
	GipsyX-FID	9.34 ± 0.67	3.45 ± 0.74	–59.4 ± 12.1	1.16 ± 0.48	122.1 ± 22.5
	GipsyX-NNR	9.14 ± 0.66	3.19 ± 0.68	–39.9 ± 11.9	1.12 ± 0.45	124.2 ± 21.6
	GipsyX-UNR	9.13 ± 0.65	3.17 ± 0.66	–39.9 ± 11.8	1.11 ± 0.44	125.5 ± 21.6
	GipsyX-JPL	9.39 ± 0.65	3.44 ± 0.66	–27.7 ± 10.9	1.17 ± 0.44	153.2 ± 20.8
	ITRF2014	9.34 ± 0.98	4.37 ± 0.78	–47.7 ± 10.1	1.17 ± 0.50	156.1 ± 23.0
	Gamit-NMA (CM)	9.52 ± 0.35	3.60 ± 0.37	–52.9 ± 5.9	0.96 ± 0.26	102.8 ± 15.3
	GipsyX-FID (CM)	9.67 ± 0.33	3.34 ± 0.38	–63.9 ± 6.5	1.17 ± 0.28	122.9 ± 13.4
	GipsyX-NNR (CM)	9.75 ± 0.34	3.45 ± 0.36	–68.1 ± 6.0	1.11 ± 0.26	120.6 ± 13.4
NYALES20	Where	8.87 ± 0.17	2.62 ± 0.80	–67.3 ± 17.9	1.14 ± 0.81	77.3 ± 31.5
NYAL-SCG		*2.52 ± 0.64	*14.38 ± 0.67	–83.8 ± 2.7	*3.92 ± 0.47	60.6 ± 6.8
Ny-Ålesund	NTL	0.92 ± 0.30	4.00 ± 0.32	–82.5 ± 4.6	1.21 ± 0.22	111.3 ±10.3
BJOS	Gamit-NMA	0.10 ± 0.54	3.30 ± 0.55	32.6 ± 9.5	1.14 ± 0.38	33.6 ± 18.4
	GipsyX-FID	–0.27 ± 0.62	0.90 ± 0.47	21.2 ± 27.3	0.62 ± 0.32	45.5 ± 27.5
	GipsyX-NNR	–0.47 ± 0.59	1.63 ± 0.58	46.1 ± 19.6	0.57 ± 0.30	–54.0 ± 27.6
Bear Island	NTL	–0.04 ± 0.31	1.99 ± 0.32	–107.7 ± 9.1	0.38 ± 0.18	100.1 ±25.3

To CM filter a time-series where the signal from a loading model is removed, the loading signal for the station(s) used in the CM filtering has to be removed as well. In our case, the loading signal was subtracted both for the BJOS time-series before computing the CM signal and for the other Svalbard time-series before the CM filtering. The final Svalbard time-series are cleaned for both the regional CM signal over Svalbard and Bear Island and the estimated load signal. The CM filtered time-series for station *i* is then:

$$H^i_{\mathrm{CM},L}(t) = H^i_{\mathrm{GNSS}}(t) - H^i_L(t) - \mathrm{CM}(t), \tag{6}$$

where *t* is the epoch, H^i_{GNSS} is the observed time-series, H^i_L is the estimated loading signal, and *CM* is the common mode signal. As described earlier, we use the time-series from BJOS to estimate the CM signal, but since we remove the estimated loading signal from the time-series, we have to remove the loading signal from BJOS time-series before computing the CM signal. Therefore, we get

$$H^i_{\mathrm{CM},L}(t) = H^i_{\mathrm{GNSS}}(t) - H^i_L(t) - (H^{\mathrm{BJOS}}_{\mathrm{GNSS}}(t) - H^{\mathrm{BJOS}}_L(t)). \tag{7}$$

2.7 Isolating the elastic signal from glacier and snow

The signal in $H_{\mathrm{CM},L}(t)$ (eq. 7) includes all vertical motions not accounted for in the loading models or CM filtering, for example unmodelled loading, Glacial Isostatic Adjustment (GIA), tectonics, and noise. Assuming that the GIA and the tectonic component are linear, the left hand side can be written $H_{\mathrm{CM},L}(t) = LIN(t) + \varepsilon(t)$, where *LIN* is the linear part and ε contains the noise. The noise includes unmodeled loadings, but also station dependent effects like multipath, atmospheric effects, not use of individual antenna calibration, and thermal expansion of antenna monument. Possible unique unmodelled signal from BJOS will also map into the noise term. Splitting the load signal into a signal from glacier and snow, H_{GS}, and other non-tidal loadings, H_{NTL^*}, we can rewrite eq. (7) into:

$$\begin{aligned} LIN^i(t) + H^i_{\mathrm{GS}}(t) + \varepsilon(t) = {} & H^i_{\mathrm{GNSS}}(t) - H^i_{\mathrm{NTL}^*}(t) \\ & - \left(H^{\mathrm{BJOS}}_{\mathrm{GNSS}}(t) - H^{\mathrm{BJOS}}_{\mathrm{NTL}^*}(t)\right. \\ & \left. - H^{\mathrm{BJOS}}_{\mathrm{GS}}(t)\right), \end{aligned} \tag{8}$$

that is we have isolated the linear part and the elastic signal from glaciers and snow as a sum of known terms.

3 RESULTS AND DISCUSSION

The vertical component of the different GNSS solutions in Ny-Ålesund and Bear Island as well as the NTL signal are included in Table 4. In addition, the Where results (Solution s1) from the NYALES20 VLBI antenna and the SCG in Ny-Ålesund are included. Some of the time-series are plotted in Fig. 6. The horizontal components of the different GNSS solutions are included in Table A1. The loading signals for all the different loading models are included in Table A2.

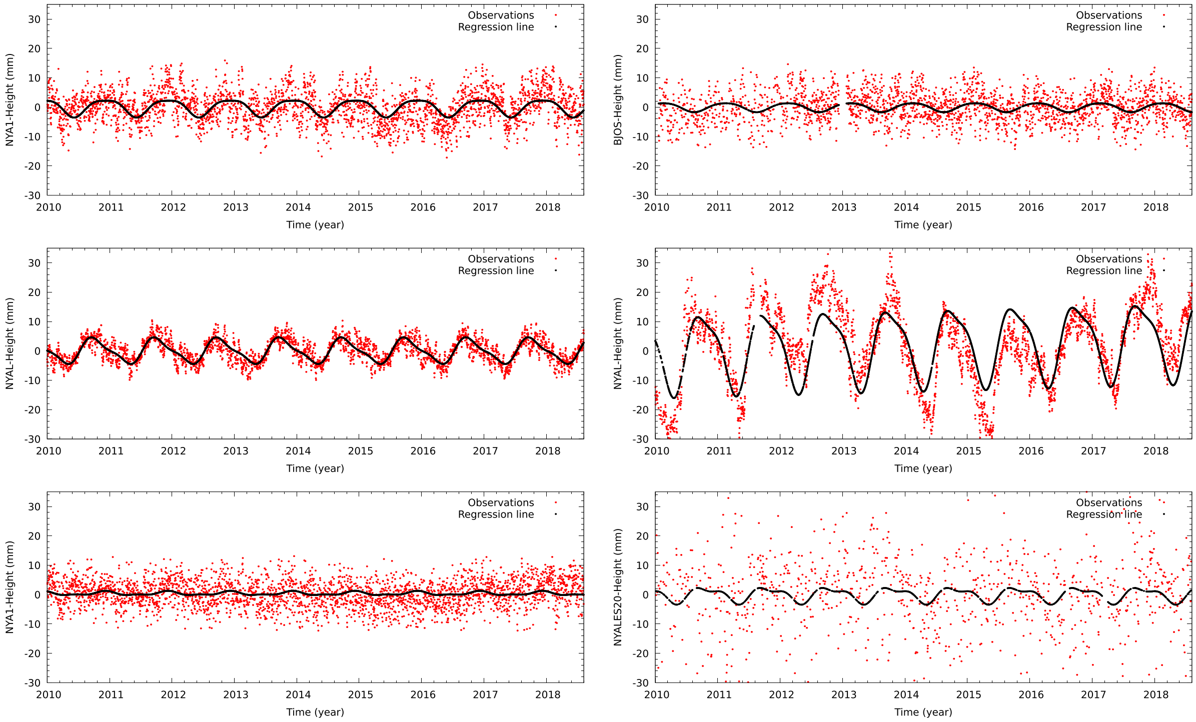

Figure 6. A selected set of detrended time-series for Svalbard. The time-series are: GipsyX-NNR for NYA1 (upper left-hand panel), NTL (ATM, NTO, LWS including the glaciers and snow) signal in Ny-Ålesund (middle left-hand panel), the GipsyX-NNR time-series for NYA1 after removal of NTL and CM filtering (lower left-hand panel), GipsyX-NNR for BJOS (upper right-hand panel), gravity from the SCG in Ny-Ålesund (middle right-hand panel) and the NYALES20 Where solution (lower right-hand panel). The gravity values are converted to millimeter using the convertion ratio –0.24 μGal mm^{-1} (Mémin *et al.* 2012).

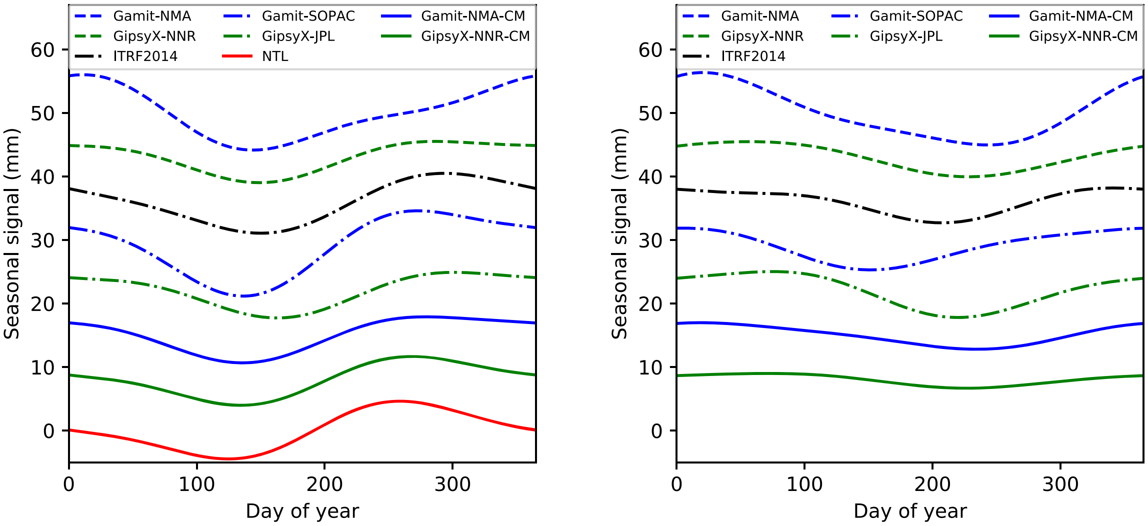

Figure 7. Seasonal signal in Ny-Ålesund (NYA1). The left-hand panel shows the sum of the annual and semi-annual sinusoidal signal for the time-series, the right-hand panel shows the same results relative to the NTL signal (ATM, NTO, LWS including the glaciers and snow). The upper most five curves are from time-series analysis of the raw time-series. The sixth and seventh curves are CM-filtered time-series. The bottom curve of the left panel is the estimated NTL signal. The curves are shifted with respect to each other to improve readability.

3.1 Determination of the loading annual signal

As shown in Kierulf *et al.* (2009b) the uplift in Ny-Ålesund varies from year to year. Consequently, trends from different time periods can not be compared directly. We have chosen to use the time interval 2010 until 2018 for time-series analysis, except for the ITRF2014 time-series that ended in 2014. The estimated uplift for the Ny-Ålesund stations agree below the uncertainty level.

The annual signal in Ny-Ålesund varies between the solutions both in phase and amplitude (Table 4, Table A1 and Fig. 7). This implies that the choice of GNSS analysis strategy has a noticeable impact on the estimated seasonal variations. Martens *et al.* (2020)

Table 5. Admittance factors for the vertical component of GNSS station in Svalbard caused by the glacier and snow loading. ADM_SEA and ADM_IAV show estimates of the seasonal and interannual admittance factors.

Station	ADM_SEA	ADM_IAV
SVES	0.94 ± 0.15	0.04 ± 0.13
NYAL	1.33 ± 0.18	0.03 ± 0.17
NYA1	1.01 ± 0.18	0.19 ± 0.16
LYRS	0.95 ± 0.18	–0.11 ± 0.21
HORN	1.35 ± 0.16	0.25 ± 0.17
All	1.12 ± 0.07	0.11 ± 0.07

found similar differences in the estimated annual signal when they compared GNSS time-series, in United States and Alaska, based on different analysis strategies. Such variations make direct geophysical interpretation of the periodicity in GNSS time-series difficult.

The measured vertical annual signal (Table 4) is smaller than the estimated NTL signal for the GipsyX solutions and larger than the estimated NTL signal for the Gamit solutions. The phase of the GNSS solutions are delayed relative to the NTL signal with between 30° and 70° (corresponding to a delay between 1 and 2.5 months) in Ny-Ålesund.

The CM-filtered solutions are closer to the expected signal from NTL and we have less differences between the GipsyX and Gamit solutions (see Fig. 7). The annual signal found with the Where software for VLBI has a smaller amplitude, but the phase is close to the phase estimated from the loading modeling.

The phase of the gravity signal in Ny-Ålesund is close to the phase of the loading models. The annual amplitude in gravity is 3.45 μGal. For a spherical and compressible Earth model the elastic gravity variations can be converted to vertical position variations using a ratio of $-0.24\ \ \mu\mathrm{Gal\,mm}^{-1}$ (Mémin *et al.* 2012). Using this ratio we got an yearly amplitude of 14.4 mm. This is much larger than the estimated annual loading signal of around 4.0 mm in Ny-Ålesund. However, the gravity variations also depends on the direct gravitational attraction. Mémin *et al.* (2012) discussed how the location of the load affect the ratio between gravity and uplift. Both the distance to and the relative height of the load have an impact. The large annual signal implies mass changes at locations with negative relative heights close to the station.

The SCG-instrument in Ny-Ålesund gives a combined signal from three glacier related factors. The viscoelastic response from past ice mass changes, the immediate elastic response of the ongoing ice mass changes, and the direct gravitational attraction from the ongoing ice mass changes on the glaciers (see Mémin *et al.* 2014; Breili *et al.* 2017). The two latter have a clear influence on the annual signal. In addition, soil moisture and accumulated snow close to and mainly below the gravimeter, have a much stronger effect on gravity than on displacements.

Quantifying the gravity signal from these nearby hydrological factors are demanding and out of the scope of this paper. However, they, as well as glaciers, are forced by temperature and precipitation. We assume that they are in phase with the elastic uplift signal. A gravimeter measures gravity changes directly, while VLBI and GNSS evaluate site positions from analysis of observations at a network, and a position estimate of a given station in general depends on measurements at other stations of the network. The phase of the SCG time-series is therefore an independent measure of the variations in Ny-Ålesund and the result coincides with the results from the other techniques.

3.2 Determination of the loading admittance factors

We found the admittance factor from VLBI solutions for the seasonal vertical displacement does not deviate from 1.0 at a 2σ level, that is the LWS signal is fully recovered from the data. At the same time the departure of the admittance factor from 1.0 for the horizontal loading components implies there is a statically significant discrepancy between the computed loading signal and the data. It should be noted that the magnitude of the seasonal signal in North direction is only 0.15 mm and the signal itself is just too small to be detected. The admittance factor for the interannual signal is significantly different from 1.0, which indicates that the loading signal alone cannot explain it.

We made an additional analysis to find the admittance factor for the glacier and snow loading signal at the GNSS stations in Svalbard. We computed mass loading for all the GNSS stations in Svalbard and fitted it to the GNSS time-series using reciprocal formal uncertainties as weights. Then we computed the χ^2 per degree of freedom of the fit and scaled variances of admittance factor estimates by this amount. Table 5 shows the estimates of the admittance factor from the differenced GNSS time-series using eq. (8). Similar to the VLBI case, the admittance is very close to 1.0 for the vertical seasonal signal (row 'All') and it is far away from 1.0 for the interannual signal and the horizontal signal.

Two factors may cause poor modeling of the interannual signal. First, calving and frontal ablation are not included in the CMB model, and therefore, lacks this contribution. Secondly, other loadings, for instance non-tidal ocean loading may contribute. The seasonal signal has a very specific time dependence pattern, and the approach of admittance factor estimation exploits the uniqueness of this pattern, while the pattern of the interannual signal is more general.

The analysis of the admittance factors give several important results in addition to the very good agreement between the different estimated vertical seasonal components. Analysis of observations shows that the CMB model provides prediction of the vertical mass loading with 1σ errors of 5 per cent, which corresponds to 0.1 mm. We have a bias wrt to the model of 0.2 ± 0.1 mm, and this bias is not statistically significant at a 95 per cent level (2σ). We conclude that analysis of the data from two totally independent techniques, VLBI and GNSS, proves there is no statistically significant deviation at a 95 per cent significance level between the seasonal vertical mass loading signal based on the CMB model and observations of both techniques.

3.3 Geodynamic interpretation

To study the time-series ability to capture the loading signal from glaciers and snowpack changes, we used the CM filtered time-series. Other known loading signals were removed using eq. (8). To have more robust time-series, in the following discussion, we have used averaged GNSS time-series. The averaged time-series are the weighted mean of the daily values from the Gamit-NMA, the GipsyX-NNR and the GipsyX-FID solutions. The annual periodic signal and the linear rate for the time-series in eq. (8) are included in Table 6 together with the elastic signal from glaciers and snow. Detailed results for the individual GNSS solutions are included in Table A3.

The amplitudes of the estimated loading signal from glaciers and snowpack vary with latitude and longitude and depend on the amount of surrounding glaciers and land masses (see Fig. 9). The station HAGN in the middle of the glacier Kongsvegen has the

Table 6. Vertical rate and annual signal for GNSS stations in Svalbard. GS are the elastic loading signal from ice and snow. GNSS-CM is the time-series using eq. (8). Max uplift is the date of the maximum value for the annual signal.

Station		Trend (mm yr^{-1})	Amp. (mm)	Pha. (°)	Max uplift (date)
Up:					
NYA1	GNSS-CML	9.74 ± 0.27	3.37 ± 0.29	–56.5 ± 5.0	3 Nov.
	GS	0.93 ± 0.03	2.66 ± 0.03	–81.8 ± 0.6	9 Oct.
NYAL	GNSS-CML	9.57 ± 0.27	3.63 ± 0.29	–67.9 ± 4.6	23 Oct.
	GS	0.93 ± 0.03	2.66 ± 0.03	–81.8 ± 0.6	9 Oct.
HAGN	GNSS-CML	11.95 ± 0.56	4.28 ± 0.65	–50.2 ± 8.6	10 Nov.
	GS	1.81 ± 0.04	3.73 ± 0.04	–80.1 ± 0.7	10 Oct.
LYRS	GNSS-CML	8.16 ± 0.42	3.21 ± 0.45	–80.8 ± 8.0	10 Oct.
	GS	0.83 ± 0.03	3.21 ± 0.03	–83.2 ± 0.6	7 Oct.
SVES	GNSS-CML	6.21 ± 0.45	3.37 ± 0.47	–96.8 ± 7.9	23 Sep.
	GS	0.86 ± 0.04	3.53 ± 0.04	–81.9 ± 0.6	8 Oct.
HORN	GNSS-CML	9.45 ± 0.27	3.21 ± 0.30	–60.0 ± 5.3	31 Oct.
	GS	1.93 ± 0.03	2.69 ± 0.03	–77.0 ± 0.6	13 Oct.
North:					
NYA1	GNSS-CML	14.98 ± 0.09	0.24 ± 0.09	39.6 ± 21.1	9 Feb.
	GS	0.56 ± 0.01	0.17 ± 0.01	–72.0 ± 1.0	18 Oct.
NYAL	GNSS-CML	14.84 ± 0.12	0.47 ± 0.12	–89.5 ± 14.9	1 Oct.
	GS	0.56 ± 0.01	0.17 ± 0.01	–72.0 ± 1.0	18 Oct.
HAGN	GNSS-CML	14.73 ± 0.36	0.83 ± 0.34	147.7 ± 22.2	29 May.
	GS	0.53 ± 0.01	0.05 ± 0.01	–49.1 ± 3.4	11 Nov.
LYRS	GNSS-CML	14.47 ± 0.16	1.19 ± 0.17	63.6 ± 8.2	5 Mar.
	GS	0.24 ± 0.01	0.06 ± 0.01	84.4 ± 3.6	26 Mar.
SVES	GNSS-CML	14.49 ± 0.33	2.55 ± 0.33	35.4 ± 7.3	4 Feb.
	GS	0.19 ± 0.01	0.24 ± 0.01	89.0 ± 1.2	31 Mar.
HORN	GNSS-CML	13.20 ± 0.14	1.02 ± 0.14	91.7 ± 8.0	2 Apr.
	GS	–0.43 ± 0.01	0.73 ± 0.01	101.6 ± 0.7	13 Apr.
East:					
NYA1	GNSS-CML	10.24 ± 0.08	0.42 ± 0.09	18.6 ± 11.8	18 Jan.
	GS	–0.07 ± 0.01	0.64 ± 0.01	98.3 ± 0.8	9 Apr.
NYAL	GNSS-CML	10.01 ± 0.08	0.16 ± 0.07	–59.1 ± 25.0	1 Nov.
	GS	–0.07 ± 0.01	0.64 ± 0.01	98.3 ± 0.8	9 Apr.
HAGN	GNSS-CML	12.65 ± 0.32	0.66 ± 0.29	151.4 ± 23.9	2 Jun.
	GS	0.32 ± 0.01	0.40 ± 0.01	94.5 ± 0.9	5 Apr.
LYRS	GNSS-CML	12.48 ± 0.17	0.35 ± 0.15	77.7 ± 23.5	19 Mar.
	GS	0.08 ± 0.01	0.27 ± 0.01	95.9 ± 1.1	7 Apr.
SVES	GNSS-CML	15.71 ± 0.27	0.76 ± 0.26	31.9 ± 18.8	1 Feb.
	GS	–0.17 ± 0.01	0.07 ± 0.01	117.7 ± 2.5	29 Apr.
HORN	GNSS-CML	11.56 ± 0.11	0.45 ± 0.11	51.2 ± 13.8	20 Feb.
	GS	–0.31 ± 0.01	0.32 ± 0.01	106.4 ± 0.9	17 Apr.

largest estimated annual loading signal, while the westernmost stations NYAL/NYA1 and HORN have the smallest. The GNSS stations SVES and LYRS are located in central parts of Svalbard and here the measured vertical annual signal agrees with the estimated loading signal at the uncertainty level. For the stations closest to the west coast NYAL, NYA1 and HORN the measured amplitudes are slightly larger than expected from the variations in glaciers and snow (~0.7, ~1.0 and ~0.5 mm, respectively). Although the admittance factor for all stations combined show very good agreement for the seasonal component, the admittance factor for individual stations in Ny-Ålesund and Hornsund are slightly above one, implying that the observed amplitude is somewhat larger than the prediction from the CMB model.

The larger vertical amplitude at NYAL, NYA1 and HORN might be due to lower precision of the CMB models in areas with more variable coastal climate, changes in groundwater and surface hydrology, and seasonal variability in calving/frontal ablation of glaciers. Especially, calving is assumed to be seasonally dependent with higher incidents during summer (when ice flows faster). This may explain a higher observed amplitude in areas like Ny-Ålesund and Hornsund, which have a lot of nearby large calving glaciers. However, the deviation of admittance factors from 1.0 for these stations is still within 2σ of the statistical uncertainty. Longer time-series are needed to establish whether there is a statistically significant deviation of observations from the model for these individual stations.

The phase of the vertical loading signal from glaciers and snow varies with only a few days over Svalbard, and corresponds to a maximal value after the end of the melting season, in mid-October. The phase of the GNSS time-series agrees with the glaciers and snow signal from the CMB models within a few weeks.

The predicted horizontal seasonal signal is smaller. It is around 0.2 mm in the north component for all locations except HORN. HORN is located in the south of Svalbard with the majority of glaciers located to the north. Consequently the north amplitude is larger, 0.7 mm. The other stations have glaciers both to the north and to the south and the loading signals are cancelled out. The east annual signal varies from 0.7 mm (NYAL, NYA1) to 0.0 mm (SVES), depending on their locations relative to the glaciers.

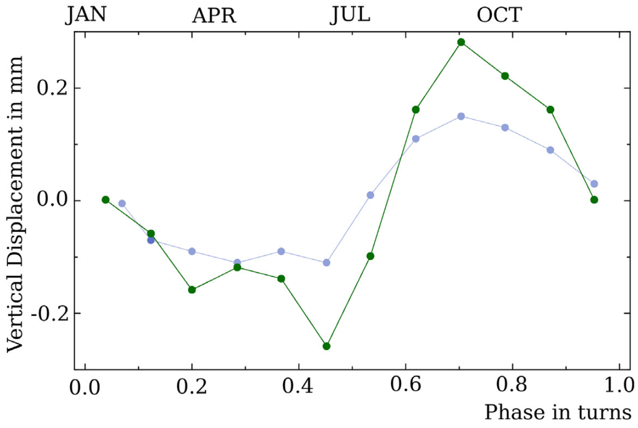

Figure 8. The seasonal contribution of glaciers in Greenland to the vertical displacement of NYALES20 after removal of the slowly varying constituent from processing GRACE data. The green line shows the total contribution, the shadowed blue line shows the residual contribution after subtraction of land water storage pressure from MERRA2 model. The horizontal axis is a phase of the seasonal signal in phase turns.

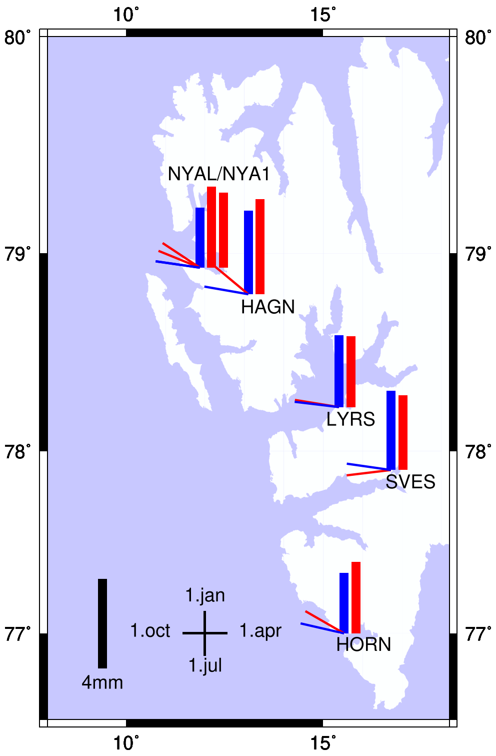

Figure 9. Annual signal for GNSS stations in Svalbard. The bars are the amplitude and the vectors are the phase. Blue is from the loading prediction from glaciers and snow red is from the GNSS stations.

We see that the estimated annual signal for the GNSS stations NYA1, HAGN, LYRS and HORN agree at 2σ level in the east component. HORN is capturing the larger north annual signal for this location. However, the small north signals for the other stations are too small to be detected. LYRS and SVES have a large north annual signal, 1.1 mm resp. 2.3 mm larger than expected loading signal. We have not established the origin of this discrepancies. Possible reasons are uneven thermal expansion of the antenna monument (steel mast) and artefacts of the atmosphere model. We will investigate these signals in the future.

Our CMB model is limited by Svalbard archipelago. Glacial loading at other islands, such as Iceland and Greenland, can bring a noticeable contribution (Kierulf *et al.* 2021, Coulson *et al.* 2021). Using Green's function from the ocean tide loading provide of Scherneck (1991),[1] assuming 100 Gt seasonal ice cycle on Greenland (see Fig. 6 in Bevis *et al.* 2012), and the average distance from Greenland to Svalbard of 800 km, we get coarse estimate of the the amplitude of mass loading signal Svalbard due to glacier in Greenland: 0.38 mm. In order to get a more refined estimate of the magnitude of such a contribution, we used Loomis *et al.* (2019) mascon solution for Greenland for 2008 from processing GRACE mission. The mascon for Greenland at a regular grid $0.5^\circ \times 0.5^\circ$ is provided[2] with a monthly resolution in the height of the column of water equivalent that covers the entire land and is zero otherwise. The mascon excludes the contribution of the atmosphere and ocean but retains the contribution of land water, snow, and ice storage.

We have converted the height of the column of water equivalent to surface pressure and computed the mass loading from the mascon using the same approach as we used for computing atmospheric and land water storage loading using spherical harmonic transform of degree/order 2699. Since MERRA2 land water storage model covers Greenland, we computed mass loading two times: the first time using the total surface pressure from the mascon and the second time after subtracting the pressure anomaly from MERRA2. In the latter case the resulting mass loading signal provides a correction to the mass loading from MERRA2 model for the contribution of glacier derived from GRACE data analysis since MERRA2 has large errors of modeling glacier dynamics. The results are shown in Fig. 8 after removal linear trend. The residual signal has amplitude 0.15 mm and is in phase with the mass loading signal from Svalbard glacier while the total signal has amplitude 0.28 mm. This estimate agrees remarkably well with our coarse estimate. Accounting for the contribution of glacier mass loading using GRACE data reduces the admittance factor from 1.10 to 1.04 for the seasonal vertical component of the VLBI solution.

We exercise a caution in results of processing GRACE data, A thorough analysis of systematic errors of mass loading signal from GRACE mascon solution requires significant efforts and is beyond the scope of the present manuscript. However, our estimates shows that the contribution of glaciers in Greenland is not dominated and its accounting improves the agreement of the CMB model with VLBI and GNSS observations.

3.4 CMB model and time-series

In the previous section we examined how the different GNSS time-series were able to capture the elastic loading signal from local ice and snow changes. In this paragraph we will discuss the effect of removing the loading signal from the time-series, both on the unfiltered time-series and the CM filtered time-series. We will in particular look at the effect of replacing the global hydrological model with a regional CMB model. In the discussion we used an averaged time-series from the GNSS solutions; Gamit-NMA, GipsyX-FID and GipsyX-NNR. Due to limited observations during winter the HAGN time-series are not directly comparable with the other time-series and therefore not included in this discussion.

[1] Fig. 2 in http://holt.oso.chalmers.se/loading/loadingprimer.html

[2] Available at https://earth.gsfc.nasa.gov/geo/data/grace-mascons

Table 7. Yearly amplitude and RMS in the time-series. In each column the three parameters are amplitude of yearly signal in mm, RMS of the time-series in mm and changes in RMS relative to the unfiltered time-series in percent. The numbers are in mm. H_{GNSS}, L_i and H_{CM,L_i} are explained in the text.

Station	H_{GNSS}	$H_{\mathrm{GNSS}} - L_1$	$H_{\mathrm{GNSS}} - L_2$	H_{CM}	H_{CM,L_1}	H_{CM,L_2}
BJOS	1.3/4.9 (0%)	2.9/4.1 (–16%)	3.0/4.1 (–16%)			
NYA1	3.8/4.6 (0%)	3.7/4.0 (–13%)	3.7/3.9 (–16%)	3.4/4.7 (2%)	2.5/4.5 (–3%)	1.5/4.4 (–4%)
NYAL	3.6/4.6 (0%)	3.1/4.1 (–12%)	3.0/3.9 (–15%)	3.4/4.7 (3%)	2.5/4.5 (–3%)	1.3/4.4 (–4%)
LYRS	3.0/6.8 (0%)	2.4/6.3 (–8%)	2.9/6.2 (–10%)	2.9/6.7 (–1%)	1.7/6.6 (–3%)	0.6/6.6 (–4%)
SVES	2.5/6.5 (0%)	1.7/5.8 (–9%)	2.8/5.7 (–11%)	2.9/6.3 (–2%)	1.5/6.1 (–5%)	1.1/6.0 (–7%)
HORN	3.3/4.7 (0%)	3.3/4.1 (–14%)	3.4/3.8 (–20%)	3.0/4.7 (–0%)	2.4/4.5 (–5%)	1.0/4.3 (–9%)

We have used time-series where no loading models where removed and two time-series with slightly different loading time-series removed (L_1, L_2). The first loading model, L_1, is the sum of the loadings from ATM, NTO and the total LWS signal from the merra2 model. The second loading model, L_2, equals L_1 except that the regional LWS signal in merra2 is replaced with the glacier and snow signal in the CMB model using eq. (2).

$H_{\mathrm{GNSS}} - L_i$ contains the unmodeled signal in the GNSS time-series after removing the modeled loadings, L_i. The signal can be presented as a sum of linear trend (from e.g. GIA and tectonics) and noise including unmodeled loading signals. That is $H_{\mathrm{GNSS}}(t) - L_i(t) = LIN(t) + \varepsilon(t)$. Also the CM filtered time-series (H_{CM}, eq. 6) and the CM filtered time-series where the loading signal is removed (H_{CM,L_i}, eq. 7) can be presented as a sum $LIN(t) + \varepsilon(t)$. To examine the quality of the time-series using different filtering and loading models we estimate the root mean square (RMS) and annual signal in the noise time-series $\varepsilon(t)$. The annual signal in $\varepsilon(t)$ is the remaining annual signal after removing the loading model L_i. A large annual signal in $\varepsilon(t)$ indicate that we have remaining unmodelled periodic signal in the time-series after removing load L_i. The RMS is a measure of the remaining noise in the time-series. The results for the averaged time-series are included in Table 7. Results for the individual solutions are included in Table A4.

We see that removal of the loading signal reduce the RMS values on average by 11 per cent, while replacing the regional hydrological signal with a CMB model reduce the RMS with 13 per cent. The improvements for the CM filtered time-series are less, 4 and 6 per cent, respectively. The removal of the CM eliminates part of the elastic loading signal, and this may explains the lower reduction for these series. Both for the unfiltered and the CM filtered time-series the RMS are reduced with 2–3 per cent when we replace the regional signal in the merra2 with the glacier and snow signal from the CMB model. The RMSs are very little affected by the CM filtering (4th vers. 1st column in Table 7).

Removing the NTL (ATM, NTO and LWS including the glaciers and snow) from the observed time-series have an effect on the daily noise scatter (RMS), but very little effect on the annual signal. This implies that removal of the NTL reduces the daily scatter in the GNSS time-series. It also implies that the periodic signal is dominated by other factors. As we saw in Section 3 this annual signal depends on the analysis strategy. We conclude that we have an analysis strategy dependent effect in the periodic signal.

The amplitude of the time-series is reduced after the CM filtering. The amplitude of the annual signal in the CM filtered time-series using load models L_1 is reduced to 2.1 mm. The largest effects are when we use load model L_2 and the CM filtered time-series. For this solution the averaged annual loading signal is 1.1 mm, one third of most other combinations of filtering and loading models.

For the horizontal components including CM filtering and removing the NTL affects the RMS only marginaly. The amplitude of the horizontal seasonal signal reduces from on average 0.6 to 0.4mm for NYAL, NYA1 and HORN when both CM filtering and NTL loadings are removed. The stations LYRS and SVES have much larger amplitudes and no improvements after filtering.

Note, the glacier model used in this study is not able to capture glacier dynamics like continuous flow of ice towards the glacier front, or more dramatic phenomena such as glacier surging (see e.g. Morris *et al.* 2020; Dunse *et al.* 2015). These dynamic effects provide a significant contribution to the total glacier mass balance and uplift, especially, on timescales from years and longer (see Kierulf *et al.* 2009b, for more on the effect of glacier dynamics on the uplift). The linear elastic uplift signal from the CMB models is not sufficient to fully describe the elastic uplift from ice and snow changes over longer timescales.

4 CONCLUSIONS

In the introduction two questions were asked: (1) How well do GNSS and VLBI capture the seasonal loading signal from glaciers and snow on Svalbard? (2) Will refining the LWS models with a CMB model improve the loading predictions? To answer these questions a network of seven permanent GNSS stations were analysed with different analysis strategies and softwares. The different time-series were studied and compared with loading predictions from ATM, NTO, LWS including glaciers and snow.

We found large discrepancies between the different analysis strategies, both in phase and amplitude, while the estimates of long-term trend were more consistent. This implies that a direct geophysical interpretation of raw GNSS time-series is problematic. To overcome this problem, we performed CM filtering utilizing the data from the nearby station at Bear Island. The elastic loading signal was removed from the time-series before the CM filtering. The CM filtered time-series gave a much better agreement. This confirmed our initial conjecture that the origin of the discrepancies in the raw time-series are due to differences in the analysis strategy in the GNSS data processing. The agreement of CM filtered time-series strengthened our confidence that we investigated a real geophysical signal, and not artefacts of data analysis.

We have decomposed the LWS signal into the seasonal and inter-annual signals, and estimated admittance factors from VLBI data and GNSS CM filtered time-series. The admittance factors estimates from vertical seasonal constituents for both techniques do not deviate from 1.0 at a 2σ level. Therefore, we conclude that the entire mass loading signal is present in data from totally independent technique at a statistical significance level of 95 per cent. The 1σ uncertainty of admittance factors corresponds to 0.1 mm. This implies that by using the CMB model we can predict seasonal vertical mass loading displacements on Svalbard with the same level of accuracy, and that predicted errors are less than the observation errors. The interannual loading signal was not recovered from observations. Further work is required to explain these discrepancies. However, since calving and frontal ablation are not included in the CMB model, they may contribute to these discrepancies.

We saw a significant reduction of residuals after subtraction of the LWS mass loading displacement. The annual amplitude was reduced from 2.1 to 1.1 mm in the CM filtered time-series. Subtraction of the LWS loading had a negligible impact on the unfiltered time-series. This provides a strong evidence that CM filtering is necessary to reveal local periodic signals when millimeter accuracy is required.

ACKNOWLEDGEMENTS

We thank the editor Prof Bert Vermeersen, Shfaqat Abbas Khan and one anonymous reviewer for their constructive comments that helped to improve the manuscript. Thanks to Zuheir Altamimi for providing the ITRF2014 time-series for the Ny-Ålesund stations. Thanks to Machiel Bos for providing the Hector software and including new features utilized in this study. We thank Bryant Loomis for providing GRACE mascon results and for a fruitful discussion. Ward van Pelt acknowledges funds from the Swedish National Space Agency (project 189/18).

DATA AVAILABILITY

The GNSS data from Hornsund (HORN) is provided by the Institute of Geophysics of the Polish Academy of Sciences (IG PAS). Time-series from SOPAC, JPL and UNR were used in the study. GNSS time-series and SCG data is available from the authors. The NTL time-series are avialable from http://massloading.net. Distributed time-series of climatic mass balance were extracted from the data set described in van Pelt *et al.* (2019).

REFERENCES

Altamimi, Z., Rebischung, P., Métivier, L. & Collilieux, X., 2016. ITRF2014: a new release of the international terrestrial reference frame modeling nonlinear station motions, *J. geophys. Res.,* **121**(8), 6109–6131.

Auriac, A., Whitehouse, P., Bentley, M., Patton, H., Lloyd, J. & Hubbard, A., 2016. Glacial isostatic adjustment associated with the barents sea ice sheet: a modelling inter-comparison, *Quater. Sci. Rev.,* **147,** 122–135.

Bertiger, W. *et al.*, 2020. GipsyX/RTGx, a new tool set for space geodetic operations and research, *Adv. Space Res.,* **66**(3), 469–489.

Bevis, M. *et al.*, 2012. Bedrock displacements in Greenland manifest ice mass variations, climate cycles and climate change, *Proc. Natl. Acad. Sci.,* **109**(30), 11 944–11 948.

Błaszczyk, M., Jania, J.A. & Hagen, J.O., 2009. Tidewater glaciers of Svalbard: recent changes and estimates of calving fluxes, *Polish Polar Res.,* **30**(2), 85–142.

Blewitt, G.W., Hammond, C. & Kreemer, C., 2018. Harnessing the GPS data explosion for interdisciplinary science, *EOS, Trans. Am. geophys. Un.,* **99,** doi:10.1029/2018EO104623.

Bock, Y. & Webb, F., 2012. *Measures Solid Earth Science ESDR System,* La Jolla, California and Pasadena, CA, USA, ftp://cddis.gsfc.nasa.gov/pub/GPS_Explorer/latest/.

Boehm, J., Werl, B. & Schuh, H., 2006. Troposphere mapping functions for GPS and very long baseline interferometry from European Centre for Medium-Range Weather Forecasts operational analysis data, *J. geophys. Res.,* **111,** B02406, doi:10.1029/2005JB003629.

Bos, M., Fernandes, R., Williams, S. & Bastos, L., 2008. Fast error analysis of continuous GPS observations., *J. Geod.,* **82,** 157–166.

Breili, K., Hougen, R., Lysaker, D.I., Omang, O. C.D. & Tangen, O.B., 2017. A new gravity laboratory in Ny-Ålesund, Svalbard, *J. Geod. Sci.,* **7**(1), 18–30.

Charlot, P. *et al.*, 2020. The third realization of the international celestial reference frame by very long baseline interferometry, *A&A,* **644,** A159.

Coulson, S., Lubeck, M., Mitrovica, J.X., Powell, E. & Hoggard, M. J., 2021,The global fingerprint ofmodern ice-mass loss on 3-D crustalmotion,*Geophysical Research Letters,***48,** 16, e2021GL095477,.

Darwin, G., 1882. On variations in the vertical due to elasticity of the Earth's surface, *Philos. Mag.,* **14**(90), 409–297.

Dunse, T., Schellenberger, T., Hagen, J.O., Kääb, A., Schuler, T.V. & Reijmer, C.H., 2015. Glacier-surge mechanisms promoted by a hydro-thermodynamic feedback to summer melt, *Cryosphere,* **9**(1), 197–215.

Gelaro, R. *et al.*, 2017. The modern-era retrospective analysis for research and applications, version 2 (merra-2), *J. Clim.,* **30**(14), 5419–5454.

Hanssen-Bauer, I., Førland, E., Hisdal, H., Mayer, S., Sandø, A. & Sorteberg, A.E., 2019. Climate in Svalbard 2100 - a knowledge base for climate adaptation, Tech. rep., NCCS Report 1.

Hartmann, T. & Wenzel, H.-G., 1995. The HW95 tidal potential catalogue, *Geophys. Res. Lett.,* **22**(24), 3553–3556.

Heflin, M. *et al.*, 2020. Automated estimation and tools to extract positions, velocities, breaks, and seasonal terms from daily GNSS measurements: illuminating nonlinear Salton trough deformation, *Earth Space Sci.,* **7**(7), doi:10.1029/2019EA000644.

Herring, T., King, R., Floyd, M. & McClusky, S., 2018. Introduction to GAMIT/GLOBK release 10.7, Tech. rep., Mass. Instit. of Technol., Cambridge.

Jungclaus, J.H. *et al.*, 2013. Characteristics of the ocean simulations in the Max Planck Institute Ocean Model (MPIOM) the ocean component of the MPI-Earth System Model, *J. Adv. Model. Earth Syst.,* **5**(2), 422–446.

Kierulf, H. P., Steffen, H., Barletta, V. R., Lidberg, M., Johansson, J., Kristiansen, O. & Tarasov, L., 2021. A GNSS velocity field for geophysical applications in Fennoscandia, *Journal of Geodynamics,* **146,**101845,.

Kierulf, H.P., Pettersen, B., McMillan, D. & Willis, P., 2009a. The kinematics of Ny-Ålesund from space geodetic data, *J. Geodyn.,* **48,** 37–46.

Kierulf, H.P., Plag, H.-P. & Kohler, J., 2009b. Measuring Surface deformation induced by present-day ice melting in Svalbard, *Geophys. J. Int.,* **179**(1), 1–13.

Kirkvik, A.-S., Hjelle, G., Dähnn, M., Fausk, I. & Mysen, E., 2017. Where—a new software for geodetic analysis, in *Proceedings of the 23rd European VLBI Group for Geodesy and Astrometry Working Meeting,* 14–19 May, Göteborg, Sweden.

Kustowski, B., Ekstöm, G. & Dziewoński, A.M., 2008. Anisotropic shear-wave velocity structure of the earth's mantle: a global model, *J. geophys. Res.,* **113**(B6).

Loomis, B.D., Luthcke, S.B. & Sabaka, T.J., 2019. Regularization and error characterization of GRACE mascons, *J. Geod.,* **93**(9), 1381–1398.

Love, A.E.H., 1911. *Some Problems of Geodynamics: Being an Essay to which the Adams Prize in the University of Cambridge was Adjudged in 1911,* Cambridge Univ. Press.

Luckman, A., Benn, D., Cottier, F., Bevan, S., Nilsen, F. & Inall, M., 2015. Calving rates at tidewater glaciers vary strongly with ocean temperature, *Nat. Commun.,* **6**(8566), doi:10.1038/ncomms9566.

Martens, H.R., Argus, D.F., Norberg, C., Blewitt, G., Herring, T.A., Moore, A.W., Hammond, W.C. & Kreemer, C., 2020. Atmospheric pressure loading in GPS positions: dependency on GPS processing methods and effect on assessment of seasonal deformation in the contiguous USA and Alaska, *J. Geod.,* **94**(12), 115, doi:10.1007/s00190–020-01445-w.

Mathews, P.M., Dehant, V. & Gipson, J.M., 1997. Tidal station displacements, *J. geophys. Res.,* **102**(B9), 20 469–20 477.

Melini, D., Gegout, P., King, M., Marzeion, B. & Spada, G., 2015. On the rebound: modeling Earth's ever-changing shape, *EOS, Trans. Am. Geophys. Un.,* **96,** doi:10.1029/2015EO033387.

Mémin, A., Boy, J. & Santamaría-Gómez, A., 2020. Correcting GPS measurements for non-tidal loading, *GPS Solut,* **24**(45), doi:10.1007/s10291-020-0959-3.

Mémin, A., Hinderer, J. & Rogister, Y., 2012. Separation of the geodetic consequences of past and present ice-mass change: influence of the topography with application to Svalbard (Norway), *Pure appl. Geophys.,* **169,** 1357–1372.

Mémin, A., Spada, G., Boy, J.-P., Rogister, Y. & Hinderer, J., 2014. Decadal geodetic variations in Ny-Ålesund (Svalbard): role of past and present ice-mass changes, *Geophys. J. Int.,* **198**(1), 285–297.

Morris, A., Moholdt, G. & Gray, L., 2020. Spread of Svalbard glacier mass loss to Barents sea margins revealed by cryosat-2, *J. geophys. Res.,* **125**(8), doi:10.1029/2019JF005357.

Noël, B. *et al.*, 2020. Low elevation of Svalbard glaciers drives high mass loss variability, *Nat. Commun.,* **11**(4597), doi:10.1038/s41467-020-18356-1.

Omang, O. C.D. & Kierulf, H.P., 2011. Past and present-day ice mass variation on Svalbard revealed by superconducting gravimeter and GPS measurements, *Geophys. Res. Lett.,* **38**(22), doi:10.1029/2011GL049266.

Petrov, L., 2017. The international mass loading service, in *REFAG 2014,* pp. 79–83, Springer International Publishing.

Petrov, L. & Boy, J.-P., 2004. Study of the atmospheric pressure loading signal in VLBI observations, *J. geophys. Res.,* **109**(B3), doi:10.1029/2003JB002500.

Plag, H. & Pearlman, M., 2009. *Global Geodetic Observing System: Meeting the Requirements of a Global Society on a Changing Planet in 2020,* Springer.

Rajner, M., 2018. Detection of ice mass variation using GNSS measurements at Svalbard, *J. Geodyn.,* **121,** 20–25.

Reichle, R.H., Koster, R.D., De Lannoy, G. J.M., Forman, B.A., Liu, Q., Sarith, P. P.M. & Touré, A., 2011. Assessment and enhancement of merra land surface hydrology estimates, *J. Clim.,* **24**(24), 6322–6338.

Sato, T., Boy, J., Tamura, Y., Matsumoto, K., Asari, K., Plag, H.-P. & Francis, O., 2006a. Gravity tide and seasonal gravity variation at Ny-Ålesund, Svalbard in Arctic, *J. Geodyn.,* **41,** 234–241.

Sato, T., Hinderer, J., MacMillan, D., Plag, H.-P., Francis, O., Falk, R. & Fokuda, Y., 2006b. A geophysical interpretation of the secular displacement and gravity rates observed at Ny-Ålesund, Svalbard in Arctic-effects of post-glacial rebound and present-day ice melting, *Geophys. J. Int.,* **165,** 729–743.

Scherneck, H.-G., 1991. A parametrized solid earth tide model and ocean tide loading effects for global geodetic baseline measurements, *Geophys. J. Int.,* **106**(3), 677–694.

van Pelt, W. *et al.*, 2019. A long-term dataset of climatic mass balance, snow conditions, and run-off in Svalbard (1957–2018), *Cryosphere,* **13**(9), 2259–2280.

van Pelt, W. J.J., Oerlemans, J., Reijmer, C.H., Pohjola, V.A., Pettersson, R. & van Angelen, J.H., 2012. Simulating melt, runoff and refreezing on Nordenskiöldbreen, Svalbard, using a coupled snow and energy balance model, *Cryosphere,* **6**(3), 641–659.

Wdowinski, S., Bock, Y., Zhang, J., Fang, P. & Genrich, J., 1997. Southern California permanent GPS geodetic array: spatial filtering of daily positions for estimating coseismic and postseismic displacements induced by the 1992 Landers earthquake, *J. geophys. Res.,* **102**(B8), 18 057–18 070.

Wenzel, H.-G., 1996. The Nanogal software: Earth tide data processing package ETERNA 3.30, *Bulletin d'Information des Marées Terrestres,* **124,** 9425–9439.

Zumberge, J.F., Heflin, M.B., Jefferson, D.C. & Watkins, M.M., 1997. Precise point positioning for the efficient and robust analysis of GPS data from large networks, *J. geophys. Res.,* **102,** 5005–5017.

APPENDIX

Table A1. Tr(end and annual signal in Ny-Ålesund and Bear Island. The parameters are estimated trend and annual signal estimated using eq. (3) for the north and east components.

Station		North			East		
		Trend (mm yr^{-1})	Amp. (mm)	Pha. (°)	Trend (mm yr^{-1})	Amp. (mm)	Pha. (°)
NYA1	Gamit-SOPAC	14.83 ± 0.12	0.26 ± 0.11	–11.5 ± 22.7	10.27 ± 0.12	1.04 ± 0.12	–6.0 ± 6.7
NYA1	Gamit-NMA	14.97 ± 0.11	0.44 ± 0.11	–61.8 ± 14.0	10.46 ± 0.10	0.61 ± 0.10	–33.2 ± 9.6
NYA1	GipsyX-FID	15.00 ± 0.13	0.67 ± 0.13	–121.4 ± 11.4	10.19 ± 0.12	1.19 ± 0.12	6.4 ± 5.8
NYA1	GipsyX-NNR	15.01 ± 0.13	0.63 ± 0.13	–116.2 ± 11.6	10.20 ± 0.11	1.08 ± 0.12	15.1 ± 6.1
NYA1	GipsyX-UNR	14.93 ± 0.13	0.64 ± 0.13	–113.7 ± 11.6	10.30 ± 0.11	1.06 ± 0.12	16.7 ± 6.4
NYA1	GipsyX-JPL	14.67 ± 0.14	0.78 ± 0.14	–108.4 ± 10.2	10.31 ± 0.13	0.85 ± 0.13	27.7 ± 8.9
NYA1	ITRF2014	14.46 ± 0.17	0.73 ± 0.14	–83.2 ± 10.7	10.40 ± 0.18	1.02 ± 0.15	2.8 ± 8.2
NYA1	Gamit-NMA (CM)	14.97 ± 0.09	0.44 ± 0.09	20.1 ± 11.9	10.50 ± 0.10	0.41 ± 0.10	–37.2 ± 14.1
NYA1	GipsyX-FID (CM)	14.98 ± 0.10	0.29 ± 0.10	18.1 ± 19.3	10.23 ± 0.09	0.41 ± 0.09	12.7 ± 13.0
NYA1	GipsyX-NNR (CM)	15.00 ± 0.09	0.34 ± 0.10	31.1 ± 16.1	10.24 ± 0.08	0.38 ± 0.09	18.4 ± 12.7
NYAL	Gamit-SOPAC	14.79 ± 0.12	0.84 ± 0.13	–79.5 ± 8.8	9.97 ± 0.11	0.47 ± 0.12	–21.8 ± 13.8
NYAL	Gamit-NMA	14.91 ± 0.12	1.12 ± 0.13	–85.6 ± 6.6	10.14 ± 0.11	0.51 ± 0.11	–95.4 ± 12.3
NYAL	GipsyX-FID	14.86 ± 0.15	1.20 ± 0.17	–114.5 ± 7.9	9.97 ± 0.13	0.90 ± 0.15	–14.2 ± 9.3
NYAL	GipsyX-NNR	14.87 ± 0.14	1.19 ± 0.15	–111.8 ± 7.1	9.99 ± 0.13	0.74 ± 0.13	0.8 ± 10.2
NYAL	GipsyX-UNR	14.86 ± 0.14	1.17 ± 0.15	–110.6 ± 7.3	10.00 ± 0.13	0.75 ± 0.13	0.9 ± 10.2
NYAL	GipsyX-JPL	14.62 ± 0.16	1.33 ± 0.16	–110.6 ± 6.9	10.00 ± 0.13	0.48 ± 0.13	12.5 ± 15.5
NYAL	ITRF2014	14.55 ± 0.21	1.20 ± 0.17	–89.9 ± 7.9	10.30 ± 0.19	0.62 ± 0.15	0.3 ± 13.4
NYAL	Gamit-NMA (CM)	14.91 ± 0.11	0.68 ± 0.11	–64.3 ± 9.5	10.18 ± 0.10	0.48 ± 0.10	–121.8 ± 12.2
NYAL	GipsyX-FID (CM)	14.84 ± 0.13	0.50 ± 0.14	–65.2 ± 15.4	10.01 ± 0.09	0.29 ± 0.10	–72.2 ± 18.7
NYAL	GipsyX-NNR (CM)	14.85 ± 0.12	0.40 ± 0.12	–71.0 ± 16.6	10.02 ± 0.09	0.19 ± 0.08	–72.3 ± 23.3
Ny-Ålesund	NTL	0.56 ± 0.04	0.35 ± 0.04	–127.3 ± 7.0	–0.04 ± 0.06	0.94 ± 0.06	59.2 ± 3.8
BJOS	Gamit-NMA	13.37 ± 0.11	0.55 ± 0.12	–110.7 ± 11.8	13.74 ± 0.13	0.29 ± 0.12	–32.7 ± 22.3
BJOS	GipsyX-FID	13.30 ± 0.16	0.94 ± 0.17	–134.2 ± 10.3	13.57 ± 0.15	0.84 ± 0.16	3.6 ± 10.6
BJOS	GipsyX-NNR	13.31 ± 0.15	0.94 ± 0.16	–128.1 ± 9.7	13.58 ± 0.15	0.74 ± 0.15	17.2 ± 11.5
Bear Island	NTL	–0.06 ± 0.05	0.45 ± 0.05	–163.0 ± 6.8	0.07 ± 0.06	0.75 ± 0.06	20.3 ± 4.7

Table A2. NTL vertical variations at GNSS stations in Svalbard. Max uplift is the date of the maximum value for the annual signal.

Station		Trend (mm yr^{-1})	Amp. (mm)	Pha. (°)	Max uplift (date)
NYA1	ATM	0.14 ± 0.14	1.02 ± 0.14	–4.1 ± 8.0	26 Dec.
	NTO	–0.06 ± 0.23	0.44 ± 0.20	167.2 ± 24.5	18 Jun.
	HYD	–0.11 ± 0.01	1.40 ± 0.01	–111.8 ± 0.3	8 Sep.
	Snowpack	–0.16 ± 0.01	0.83 ± 0.01	–89.8 ± 0.6	30 Sep.
	Ice	1.09 ± 0.02	1.84 ± 0.02	–78.3 ± 0.7	12 Oct.
	Total loads	0.92 ± 0.30	4.00 ± 0.32	–82.5 ± 4.5	8 Oct.
NYAL	ATM	0.14 ± 0.14	1.02 ± 0.14	–4.1 ± 8.0	26 Dec.
	NTO	–0.06 ± 0.23	0.44 ± 0.20	167.2 ± 24.5	18 Jun.
	HYD	–0.11 ± 0.01	1.40 ± 0.01	–111.8 ± 0.3	8 Sep.
	Snowpack	–0.16 ± 0.01	0.83 ± 0.01	–89.8 ± 0.6	30 Sep.
	Ice	1.09 ± 0.02	1.84 ± 0.02	–78.3 ± 0.7	12 Oct.
	Total loads	0.92 ± 0.30	4.00 ± 0.32	–82.5 ± 4.5	8 Oct.
HAGN	ATM	0.15 ± 0.16	1.12 ± 0.17	–3.0 ± 8.4	28 Dec.
	NTO	–0.07 ± 0.22	0.44 ± 0.20	167.7 ± 24.0	19 Jun.
	HYD	–0.10 ± 0.01	1.41 ± 0.01	–111.8 ± 0.3	8 Sep.
	Snowpack	–0.24 ± 0.01	0.81 ± 0.01	–88.3 ± 0.6	2 Oct.
	Ice	2.05 ± 0.04	2.92 ± 0.04	–77.7 ± 0.7	13 Oct.
	Total loads	1.80 ± 0.32	5.06 ± 0.33	–80.1 ± 3.7	10 Oct.
LYRS	ATM	0.15 ± 0.15	1.02 ± 0.16	–3.9 ± 8.9	27 Dec.
	NTO	–0.09 ± 0.22	0.46 ± 0.20	169.1 ± 23.6	20 Jun.
	HYD	–0.10 ± 0.01	1.45 ± 0.01	–111.9 ± 0.4	8 Sep.
	Snowpack	–0.06 ± 0.01	1.35 ± 0.01	–89.7 ± 0.6	1 Oct.
	Ice	0.89 ± 0.02	1.87 ± 0.02	–78.5 ± 0.7	12 Oct.
	Total loads	0.80 ± 0.31	4.57 ± 0.33	–84.4 ± 4.1	6 Oct.
SVES	ATM	0.15 ± 0.17	1.04 ± 0.17	–3.5 ± 9.2	27 Dec.
	NTO	–0.10 ± 0.22	0.47 ± 0.20	169.3 ± 23.3	20 Jun.
	HYD	–0.10 ± 0.01	1.48 ± 0.01	–112.0 ± 0.3	8 Sep.
	Snowpack	–0.10 ± 0.01	1.13 ± 0.01	–89.2 ± 0.6	1 Oct.
	Ice	0.95 ± 0.03	2.41 ± 0.03	–78.5 ± 0.7	12 Oct.
	Total loads	0.81 ± 0.33	4.92 ± 0.34	–83.3 ± 3.9	7 Oct.
HORN	ATM	0.13 ± 0.13	0.86 ± 0.13	–3.5 ± 8.7	27 Dec.
	NTO	–0.10 ± 0.23	0.48 ± 0.21	168.9 ± 23.7	20 Jun.
	HYD	–0.10 ± 0.01	1.50 ± 0.01	–112.0 ± 0.3	8 Sep.
	Snowpack	–0.02 ± 0.01	0.50 ± 0.01	–89.6 ± 0.7	1 Oct.
	Ice	1.95 ± 0.03	2.20 ± 0.03	–74.1 ± 0.7	16 Oct.
	Total loads	1.87 ± 0.31	4.05 ± 0.32	–82.8 ± 4.5	8 Oct.

Table A3. Vertical rate and annual signal for GNSS stations in Svalbard. The results are based on the time-series using eq. (8). Max uplift is the date of the maximum value for the annual signal.

Station		Trend (mm yr^{-1})	Amp. (mm)	Pha. (°)	Max uplift (date)
NYA1	Gamit-NMA-CML	9.51 ± 0.37	4.14 ± 0.39	–59.6 ± 5.4	31 Oct.
	GipsyX-FID-CML	9.75 ± 0.25	3.03 ± 0.28	–71.2 ± 5.2	19 Oct.
	GipsyX-NNR-CML	9.82 ± 0.28	3.20 ± 0.30	–72.8 ± 5.4	18 Oct.
	GNSS-CML	9.74 ± 0.27	3.37 ± 0.29	–56.5 ± 5.0	3 Nov.
NYAL	Gamit-NMA-CML	9.46 ± 0.32	3.74 ± 0.34	–65.5 ± 5.1	25 Oct.
	GipsyX-FID-CML	9.62 ± 0.24	3.60 ± 0.29	–77.4 ± 4.7	13 Oct.
	GipsyX-NNR-CML	9.69 ± 0.27	3.80 ± 0.29	–78.6 ± 4.4	12 Oct.
	GNSS-CML	9.57 ± 0.27	3.63 ± 0.29	–67.9 ± 4.6	23 Oct.
HAGN	Gamit-NMA-CML	12.49 ± 0.62	4.38 ± 0.68	–78.7 ± 8.8	12 Oct.
	GipsyX-FID-CML	12.39 ± 0.50	4.34 ± 0.67	–61.6 ± 8.8	29 Oct.
	GipsyX-NNR-CML	12.08 ± 0.54	4.42 ± 0.70	–61.7 ± 9.0	29 Oct.
	GNSS-CML	11.95 ± 0.56	4.28 ± 0.65	–50.2 ± 8.6	10 Nov.
LYRS	Gamit-NMA-CML	7.80 ± 0.35	3.09 ± 0.37	–53.4 ± 6.8	6 Nov.
	GipsyX-FID-CML	8.26 ± 0.37	3.00 ± 0.41	–67.1 ± 7.8	23 Oct.
	GipsyX-NNR-CML	8.20 ± 0.57	3.87 ± 0.60	-99.3 ± 8.9	21 Sep.
	GNSS-CML	8.16 ± 0.42	3.21 ± 0.45	–80.8 ± 8.0	10 Oct.
SVES	Gamit-NMA-CML	6.49 ± 0.43	3.95 ± 0.45	–80.6 ± 6.5	10 Oct.
	GipsyX-FID-CML	6.21 ± 0.45	3.46 ± 0.47	–103.5 ± 7.8	17 Sep.
	GipsyX-NNR-CML	6.27 ± 0.46	3.59 ± 0.48	–102.4 ± 7.6	18 Sep.
	GNSS-CML	6.21 ± 0.45	3.37 ± 0.47	-96.8 ± 7.9	23 Sep.
HORN	Gamit-NMA-CML	9.46 ± 0.27	3.40 ± 0.30	–55.4 ± 5.0	4 Nov.
	GipsyX-FID-CML	9.52 ± 0.25	3.58 ± 0.28	–62.6 ± 4.4	28 Oct.
	GipsyX-NNR-CML	9.59 ± 0.26	3.66 ± 0.29	–63.8 ± 4.5	27 Oct.
	GNSS-CML	9.45 ± 0.27	3.21 ± 0.30	–60.0 ± 5.3	31 Oct.

Table A4. Yearly amplitude and RMS in the time-series. In each column the three parameters are amplitude of yearly signal in mm, RMS of the time-series in mm and changes in RMS relative to the unfiltered time-series in percent. The numbers are in mm. H_{GNSS}, L_i and H_{CM,L_i} are explained in the text.

Station	H_{GNSS}	$H_{\mathrm{GNSS}} - L_1$	$H_{\mathrm{GNSS}} - L_2$	H_{CM}	H_{CM,L_1}	H_{CM,L_2}
BJOS						
Gamit_NMA	3.3/4.3 (0%)	4.9/4.3 (–0%)	5.0/4.3 (–1%)			
GipsyX_NNR	1.6/5.0 (0%)	3.3/4.2 (–15%)	3.4/4.2 (–15%)			
GipsyX_FID	0.9/5.2 (0%)	2.2/4.3 (–17%)	2.3/4.3 (–17%)			
GNSS	1.3/4.9 (0%)	2.9/4.1 (–16%)	3.0/4.1 (–16%)			
NYA1						
Gamit_NMA	5.8/4.5 (0%)	6.0/4.6 (3%)	5.8/4.5 (0%)	4.1/4.3 (–5%)	3.1/4.3 (–4%)	2.0/4.2 (–6%)
GipsyX_NNR	3.0/5.1 (0%)	3.0/4.4 (–14%)	3.3/4.2 (–16%)	2.9/5.0 (–2%)	2.0/4.6 (–8%)	0.8/4.6 (–10%)
GipsyX_FID	3.0/5.0 (0%)	2.3/4.2 (–16%)	2.4/4.1 (–18%)	2.8/5.0 (0%)	1.9/4.8 (–5%)	0.7/4.7 (–6%)
GNSS	3.8/4.6 (0%)	3.7/4.0 (–13%)	3.7/3.9 (–16%)	3.4/4.7 (2%)	2.5/4.5 (–3%)	1.5/4.4 (–4%)
NYAL						
Gamit_NMA	5.2/4.7 (0%)	5.5/4.8 (1%)	5.3/4.7 (–1%)	3.6/4.2 (–11%)	2.7/4.1 (–13%)	1.4/4.1 (–14%)
GipsyX_NNR	3.2/5.1 (0%)	2.7/4.4 (–13%)	2.7/4.3 (–16%)	3.5/5.1 (0%)	2.5/4.7 (–7%)	1.2/4.6 (-9%)
GipsyX_FID	3.4/4.9 (0%)	2.0/4.2 (–15%)	1.7/4.0 (–17%)	3.3/5.0 (3%)	2.3/4.7 (–4%)	1.1/4.6 (–6%)
GNSS	3.6/4.6 (0%)	3.1/4.1 (–12%)	3.0/3.9 (–15%)	3.4/4.7 (3%)	2.5/4.5 (–3%)	1.3/4.4 (–4%)
LYRS						
Gamit_NMA	5.3/4.8 (0%)	6.2/4.9 (3%)	6.4/4.9 (1%)	3.1/4.4 (–8%)	2.3/4.3 (–11%)	1.6/4.2 (–12%)
GipsyX_NNR	2.5/7.8 (0%)	1.6/7.3 (–7%)	2.4/7.2 (–8%)	3.4/7.8 (0%)	2.2/7.6 (–4%)	1.4/7.5 (–4%)
GipsyX_FID	3.1/7.0 (0%)	2.6/6.5 (–7%)	2.9/6.4 (–8%)	2.9/7.0 (0%)	1.8/6.9 (–2%)	0.9/6.8 (–3%)
GNSS	3.0/6.8 (0%)	2.4/6.3 (–8%)	2.9/6.2 (–10%)	2.9/6.7 (–1%)	1.7/6.6 (–3%)	0.6/6.6 (–4%)
SVES						
Gamit_NMA	4.6/5.7 (0%)	4.8/5.7 (1%)	4.9/5.6 (–1%)	3.6/5.2 (–7%)	2.3/5.1 (–10%)	0.7/4.9 (–12%)
GipsyX_NNR	2.2/6.9 (0%)	1.8/6.3 (-9%)	3.0/6.2 (–11%)	3.0/6.8 (–2%)	1.8/6.5 (–7%)	1.3/6.4 (–8%)
GipsyX_FID	2.7/6.9 (0%)	0.9/6.2 (–11%)	2.2/6.1 (–12%)	2.9/6.8 (–2%)	1.7/6.5 (–7%)	1.4/6.4 (–8%)
GNSS	2.5/6.5 (0%)	1.7/5.8 (-9%)	2.8/5.7 (–11%)	2.9/6.3 (–2%)	1.5/6.1 (–5%)	1.1/6.0 (–7%)
HORN						
Gamit_NMA	5.6/4.9 (0%)	6.0/5.1 (3%)	5.9/4.9 (–0%)	3.3/4.5 (–8%)	2.7/4.4 (–10%)	1.4/4.3 (–14%)
GipsyX_NNR	3.4/4.8 (0%)	3.4/4.1 (–14%)	3.4/3.9 (–19%)	3.3/4.8 (1%)	2.9/4.5 (–5%)	1.2/4.3 (–10%)
GipsyX_FID	3.5/4.8 (0%)	2.9/4.0 (–17%)	2.5/3.8 (–21%)	3.3/4.9 (1%)	2.8/4.7 (–3%)	1.2/4.4 (–8%)
GNSS	3.3/4.7 (0%)	3.3/4.1 (–14%)	3.4/3.8 (–20%)	3.0/4.7 (–0%)	2.4/4.5 (–5%)	1.0/4.3 (–9%)